MATERIALS CHEMISTRY
FRONTIERS

REVIEW

View Article Online
View Journal | View Issue

Cite this: *Mater. Chem. Front.*, 2023, **7**, 806

Rare earth-based MOFs for photo/electrocatalysis

Senyao Meng, Ge Li, Ping Wang, Miao He, Xiaohua Sun* and Zhenxing Li *

Received 21st November 2022,
Accepted 14th January 2023

DOI: 10.1039/d2qm01201d

rsc.li/frontiers-materials

Metal–organic frameworks (MOFs) are porous crystalline materials that have been studied and applied in the fields of energy storage, catalysis and separation. Rare earth MOFs have the advantages of MOF materials in addition to the rare earth metal ion 4f electronic layer, large orbital coupling effect, and internal magnetic anisotropy. Rare earth MOFs have higher coordination numbers and richer coordination geometries than transition metal ions as functional metal centers of MOFs. Since the 4f electron layer endows rare earth MOFs with special optical and electrical properties, they have the potential for application in photocatalysis and electrocatalysis. This review reports the current research progress on rare earth MOFs, including synthesis methods and photocatalytic and electrocatalytic applications of rare earth MOFs. We divided the different ligands into 1,4-benzene dicarboxylic acid (BDC), 1,3,5-benzenetricarboxylic acid (BTC), the zeolite imidazole framework (ZIF), and some uncommon rare earth MOFs materials. The photocatalytic and electrocatalytic applications include the oxygen reduction reaction (ORR), hydrogen evolution reaction (HER), oxygen evolution reaction (OER), CO_2 reduction reaction (CO_2RR), and other applications. Finally, we summarize the progress and existing challenges of rare earth MOF materials in the fields of photocatalysis and electrocatalysis.

1. Introduction

MOFs are a new type of porous crystal material, whose structure is mainly composed of organic ligands and metal ions. In the past years, MOFs have emerged as a novel class of porous materials that have received increasing attention for their applications in fields such as heterogeneous catalysis, biomimetic mineralization, intelligent sensors, gas storage and separation, *etc.*[1–4] Compared with traditional catalysts, the synthesis of MOFs can be flexible and there are many possibilities for the combination of metal and organic joint points. MOFs have many advantages, such as large surface area, adjustable pore structure, and multiple catalytic sites. Therefore, MOFs can provide great potential in the design of new catalyst materials.[5–7] The rare earth metals include 15 lanthanides as well as yttrium and scandium.[8,9] The unique luminescence and catalytic properties of rare earth metals make them irreplaceable and widely used in various fields. The introduction of multifunctional metal centers is a key function for MOF materials. Since rare earth metals easily coordinate with ligands

State Key Laboratory of Heavy Oil Processing, College of New Energy and Materials, China University of Petroleum (Beijing), Beijing 102249, P. R. China.
E-mail: hua82@126.com, lizx@cup.edu.cn

Senyao Meng

Senyao Meng was born in 1996 in Henan province. He obtained his Master's degree from the College of Science, China University of Petroleum (2022). Currently, he is pursuing his PhD degree at the College of New Energy and Materials, China University of Petroleum (Beijing). His research interest is in the applications of rare earth MOF in photocatalysis.

Ge Li

Ge Li was born in 1999 in Hebei Province. She received her bachelor's degree from Shijiazhuang University and is currently studying in Professor Zhenxing Li's research group at the College of New Energy and Materials, China University of Petroleum (Beijing). Her research is on the applications of polymetallic layered hydroxides in electrooxidation.

containing oxygen[10] and nitrogen,[11] especially carboxylic acid ligands,[12] and have elevated coordination numbers and diverse coordination modes, it is possible to obtain new structure MOFs. However, due to steric hindrance, rare earth elements cannot completely coordinate with ligands, leaving one or more coordination sites to coordinate with small solvent molecules to form end groups. When the synthesized rare earth MOFs are heat treated in a high vacuum for a certain period, these small molecules are discharged from the rare earth MOFs skeleton and the coordinatively unsaturated sites are exposed in the rare earth MOFs structure, which can be used as the active Lewis acid centers. Rare earth metals have similar coordination properties[13,14] and can have a variety of coordination changes. The changes in coordination number and geometric configuration only represent a small difference in energy, which opens the door to new discoveries.[15,16]

In this review, we provide the background on the current state of research on rare earth MOFs (Scheme 1). The synthesis methods of rare earth MOFs are summarized and are divided into 1,4-benzene dicarboxylic acid (BDC), 1,3,5-benzenetricarboxylic acid (BTC), zeolite imidazole framework (ZIF), and some uncommon rare earth MOFs materials, according to the different ligands. We report in detail on the applications of rare earth MOFs in photocatalysis and electrocatalysis, including HER, OER, CO_2RR, and other applications. Finally, we summarize the application studies of rare earth MOFs and present the existing challenges. Some proposed development

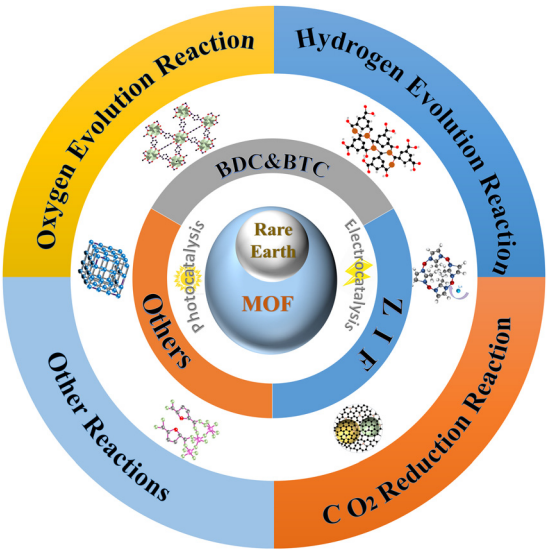

Scheme 1 Schematic diagram of the structure, synthesis, and catalytic application of rare earth-based MOFs.

Ping Wang

Ping Wang received her Master's degree from the China University of Petroleum (Beijing) in 2022. She is a PhD student under the supervision of Prof. Zhenxing Li at the College of New Energy and Materials, China University of Petroleum (Beijing), China. Her current research interests are in the synthesis and application of functional nanomaterials.

Miao He

Miao He was born in 1996 in Heilongjiang province. She received her Master's degree from the China University of Petroleum (Beijing) in 2021. She is a PhD student under the supervision of Prof. Zhenxing Li at the College of New Energy and Materials, China University of Petroleum (Beijing), China. Her current research interests are in the synthesis and application of functional nanomaterials.

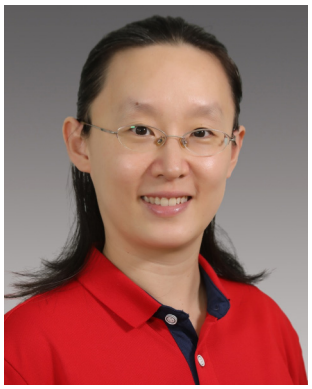

Xiaohua Sun

Xiaohua Sun obtained her PhD (2014) at the University of Cambridge. She is currently a Professor at the State Key Laboratory of Heavy Oil Processing and College of New Energy and Materials at the China University of Petroleum (Beijing). Her recent research interests focus on renewable energy, electrolytic hydrogen production, and nano self-assembly and imprint technology and its applications.

Zhenxing Li

Zhenxing Li obtained his PhD (2011) at the Peking University of China. He is currently a Professor at the State Key Laboratory of Heavy Oil Processing and College of New Energy and Materials at the China University of Petroleum (Beijing). His recent research interests focus on the design and synthesis of porous materials and rare earth-based nanomaterials for application in electrocatalysis, photocatalysis, and organic synthesis.

directions to address the problems are presented. Although our research is only a small part of the numerous rare earth MOFs materials, we hope to provide ample representation and insights into the development of this research field.

2. Synthesis

2.1. BDC & BTC

2.1.1 BDC. The compounds, dimensions, and morphologies of MOFs are the key factors affecting the photocatalytic properties.[17] For this reason, scientists have been researching efficient synthetic routes to MOFs.[18,19] The structure or morphology of the raw materials used to synthesize MOFs plays a crucial role in the final product properties. Among the different MOF ligands, terephthalic acid, also systematically known as 1,4-benzene dicarboxylic acid (BDC), has been showing remarkable properties in enhancing catalytic performance.[20,21] Furthermore, various methods have been used to improve the catalytic properties of the MOFs, such as doping metal ions in MOFs,[22] linking metal oxides,[23] sulfides[24] and phosphates[25] with MOFs, *etc.* Recently, the use of rare earth metals as modifiers or replacements for the doping of metal nodes in MOFs with BDC as ligands has attracted significant attention.[26–29] Over the past few years, many procedures, including hydrothermal and solvothermal reactions,[18,27,30] solution precipitation,[31] sonication,[20] *etc.*, have been used to efficiently synthesize MOFs. In this section, we will describe some of the achievements.

2.1.1.1 Hydrothermal method. The hydrothermal reaction is one of the most commonly used methods for synthesizing nanomaterials,[18,21,32] and the reaction is carried out by placing the reactant solution in an autoclave at high temperature and high pressure. This reaction usually yields products with good dispersion and high degrees of crystallinity. The hydrothermal reaction is an easily controlled method for effectively synthesizing MOFs.[18] However, the low synthesis yield and long reaction times are still challenging to overcome.[30] The reactions of MOFs synthesized by the hydrothermal method have not been fully studied. In 2008, with rare earth ions as the central sites and pyridine-2,3-dicarboxylic acid and benzene-1,4-dicarboxylic acid as the organic framework, a novel three-dimensional (3D) hybrid compound species was synthesized by a hydrothermal method. The structure was composed of dimer units connected by pyridine-2,3-dicarboxylate units to form a two-dimensional (2D) layered structure, supported by benzoate units to complete the formation of the 3D structure (Fig. 1a). The structure had the coordination of two reversibly adsorbed H_2O to form a one-dimensional (1D) spiral chain structure. These MOFs contain regularly conjugated π systems (benzene) and nitrogen-containing ligands (pyridine) bound to lanthanide metals. Since these two groups have strong absorption peaks in the ultraviolet (UV) spectrum, the lanthanide ions are sensitized by the antenna effect.[33–35] The transition of $\pi \rightarrow \pi^*$ or $n \rightarrow \pi^*$ electrons will lead to energy transfer in the ligand, which is manifested macroscopically as a high-intensity band observed at 300 nm in the UV-Vis spectrum.

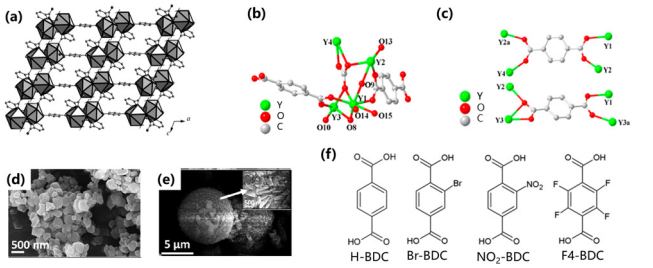

Fig. 1 (a) The 3D structure formed by the connectivity between the 2D layers and BDC units, Copyright 2008, Wiley VCH. (b) View of the asymmetric unit of $Y_{10}(C_8H_4O_4)_6(CO_3)_3(OH)_{12}$. (c) View of the coordination mode of BDC ligands, Copyright 2019, American Chemical Society. SEM image of (d) Ce–BDC and (e) Ce–BDC–NH_2, Copyright 2021, American Chemical Society. (f) Molecular structure of the linkers used. Copyright 2019, American Chemical Society.

2.1.1.2 Solvothermal method. The synthesis of MOFs with BDC as the raw material has generally been carried out by the solvothermal method.[21,36–39] The steps of the solvothermal method are basically the same as the hydrothermal method. The hydrothermal method is a chemical reaction in a solution above the boiling point of water, but the solvothermal method uses a non-aqueous liquid as a solvent at a relatively high temperature.[27] Chen *et al.* used a mixed solution of water and *N*,*N*-dimethylformamide (DMF) to perform a solvothermal reaction to introduce Eu^{3+} into the lattice of $Y_{10}(C_8H_4O_4)_6(CO_3)_3(OH)_{12}$. The formed structure consists of four Y^{3+} ions, two deprotonated BBC^{2-} and a hydroxyl group (Fig. 1b) formed by a carbonate radical in the *P*3*c*1 system to make asymmetric units. BDC ligands have two coordination modes due to the influence of the two coordination modes of the carboxyl group (*i.e.* bridging bidentate and linking/bridging tridentate) (Fig. 1c). Inorganic plates connected by BDC organic ligands as framework structures, and the products prepared solvothermally have a hexagonal layered morphology. The material substituted by Eu^{3+} exhibits fluorescence and selective quenching of Fe^{3+} makes it potentially valuable in fluorescence detection materials.[37] In 2021, Das *et al.* synthesized Ce-MOFs with (Ce–BDC–NH_2) and without (Ce–BDC) amine functionalization for CO_2 immobilization and the photocatalytic reduction of CO_2 with epoxides. Ce–BDC and Ce–BDC–NH_2 were synthesized by a solvothermal reaction, Ce–BDC was synthesized by complexation synthesis, and amine-functionalized Ce–BDC–NH_2 was synthesized in almost the same way but with different doses and solutions. Ce–BDC was a light-yellow precipitate, and after cooling to room temperature in the oven, the Ce–BDC–NH_2 product was a brown solid (Fig. 1d and e).[39] The nano-crystallite diameters of Ce–BDC-66 and Ce–BDC–NH_2 were calculated by the Scherrer formula to be 58.83 and 22.22 nm, respectively.[40]

Apart from the hydrothermal and solvothermal methods, an almost solvent-free strategy was proposed to obtain Ce-UiO-66. The initial steps were the energetic grinding of the metal salts and linkers in the presence of a small amount of acetic acid. This method controlled the liquid/solid ratio of the reactants between 0.1 and 1, similar to liquid-assisted grinding.[41]

The BDC linkers used for the synthesis of Ce-MOFs were named Ce-UiO-66-X (with X = H, Br, NO_2), Ce-UiO-66-4F, and Ce-MIL-140A-4F (Fig. 1f). Among these functional MOFs, the most stable were Ce-UiO-66-H and Ce-UiO-66-Br.[42]

2.1.2 BTC

2.1.2.1 Hydrothermal method

Synthesis of La-BTC. Jeyaseelan *et al.* studied the preparation of the hydroxyapatite (HAP) lamellar lanthanum–phenyl tricarboxylic acid–base organic skeleton template for water defluorination (Fig. 2a).[44] The nucleation and growth of La-based MOFs require layer-by-layer (LBL) techniques in HAP hard templates. HAP-La-BTC MOFs were synthesized by a template-directed LBL technique. Ethanol was removed by the centrifugation of a HAP-containing ethanol dispersant. The morphology of HAP-La-based MOFs was a rod-like porous structure, and the size was not uniform at 5 μm.

Synthesis of Ce–BTC. Zhang *et al.* prepared Ce–BTC using $(NH_4)_2Ce(NO_3)_6$ as the Ce precursor.[45] Ce–BTC showed a large number of irregular and symbiotic nanoparticles. The particle sizes ranged from 0.10 to 0.36 μm, with an average diameter of 0.23 μm.

Synthesis of Sm-BTC. Lee *et al.* prepared Sm-BTC by a hydrothermal method to solve the problem of dye-containing wastewater in the textile industry.[48] The Sm-BTC was a rod-shaped crystal, and the size was about 5 μm to 25 μm (Fig. 2c). In terms of adsorption and the absorption of Bengal rose molecules, it is superior to existing MOFs. The adsorption capacity remained high even after three adsorption–desorption cycles, and a membrane adsorber was prepared based on the growth of Sm-BTC crystals in the matrix of three porous polymer materials (nylon,[49] polyethersulfone[50] and polytetrafluoroethylene[51]). The Sm-BTC supported by nylon showed the highest adsorption performance, which may be due to the uniform distribution of crystals in the scaffold (Fig. 2d).

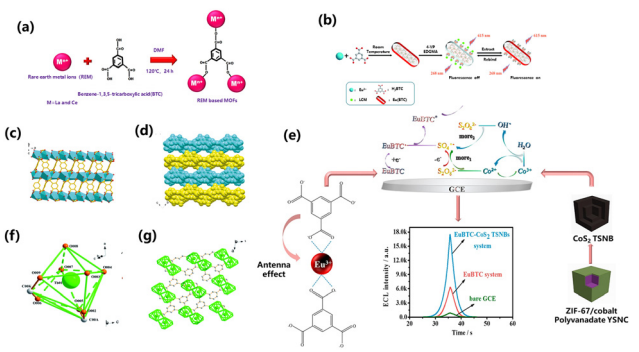

Fig. 2 (a) The possible synthesis of rare earth metal ions-based MOFs, Copyright 2021, Elsevier. (b) Preparation of Eu(BTC)-MIP, Copyright 2019, Royal Society of Chemistry. (c) Perspective view showing the layered structure of Sm-BTC. (d) A space-filling model of Sm-BTC, Copyright 2019, Royal Society of Chemistry. (e) The mechanistic illustration of increased electrochemiluminescence by the antenna effect and the dual enhancement effect of CoS_2 triple shelled nano boxes, Copyright 2021, Elsevier. (f) Coordination environment of the Tb atom. (g) 2D frame diagram of Tb-MOFs, Copyright 2022, Royal Society of Chemistry.

Synthesis of Eu-BTC. Eu-BTC was synthesized by Zhao *et al.* and had a cauliflower appearance made up of many nanorods with a width of about 500 nm, and the dense arrangement of nanorods resulted in a rich active site. A large amount of $SO^{\bullet 4-}$ reacted with Eu-$BTC^{\bullet -}$ in the holes of Eu-BTC to produce more abundant EuBTC*, thus improving the ECL efficiency (Fig. 2e).[52]

Synthesis of Gd-BTC. Garg *et al.* synthesized Gd-BTC by a solvothermal method.[53] BTC and gadolinium nitrate hexahydrate were dissolved in a mixture of DMF, ethanol and water. After the reactants were dissolved, the reaction mixture was heated for one day. The product was then cooled to room temperature and allowed to air dry. Gd-BTC had a rod-like structure, and the length of the rods was 20–30 μm. After the GD-BTC was activated, the coordination unsaturation point of Gd(III) in the organic framework formed a 1D ionic chain, and the pore size could store hydrogen. Therefore, the GD-BTC can be further applied in hydrogen adsorption measurements[54] and humidity sensing.[55]

Synthesis of Dy-BTC. Guo *et al.* prepared Dy-BTC crystals and Dy-BTC nanocrystals. Two basic parameters for the reduction of the size of the Dy-BTC to the nanoscale were revealed by studying the parameters using sodium acetate as a modulator.[58] One was to control the deprotonation of the organic bonds through the alkaline environment, which controlled the nucleation process. Another method was to use capping groups to inhibit the growth of microcrystals. Dy-BTC nanocrystals were prepared by HAc (acetic acid) + TEA (triethyl amine) and 2–5 equal amounts of acetic acid relative to BTC were added to the standard solution. After mixing, the pH value of the solution was adjusted to 5.9 with TEA. The tuning of the crystal size of Dy-BTC from micrometers to nanometers can be accomplished by adding different amounts of sodium acetate to the synthetic solution. Sodium acetate accelerated the crystal growth rate. The enhanced effect was related to the alkalinity of sodium acetate, which can increase the rate of deprotonation and thus the rate of nucleation.

Synthesis of Tm-BTC. Chinnapaiyan *et al.* reported a method for the synthesis of Tm-BTC *via* a unipolar solvent using a hydrothermal method.[25] The electrocatalytic sensing performance of edible roxarsone was investigated by using the prepared Tm-BTC-modified electrode. The Tm-BTC was white in appearance and about 1 micron in size, and the particles were dumbbell and needle-shaped.

2.1.2.2 Solvothermal method

Synthesis of La-BTC. BTC is a rigid ligand with moderate size, which easily forms a compact structure and interpenetrating structures in the coordination process with metals. Prabhu *et al.* synthesized La-BTC using lanthanum chloride as the lanthanum precursor,[43] and the shape of the La-BTC was an irregular distribution with a size of 5 μm.

Synthesis of Ce–BTC. Peng *et al.* used a solvothermal method to synthesize cerium-based organic skeletons, and

the Ce–BTC was in the form of needle-like particles with a size of 10–20 microns and small broken particles.[46] Tian *et al.* developed a way to synthesize organic frameworks for catalysis and pH-dependent selective tumor chemotherapy, and used this method to synthesize Ce-based organic frameworks. The cerium nitrate and phthalic acid were dripped separately into a flask containing H_2O through a two-channel syringe pump, and the Ce–BTC prepared by the flow process had a diameter of about 40 nm and a length in the range of several hundred nanometers.[47]

Synthesis of Eu-BTC. The Eu-BTC with high luminosity was synthesized by Wu *et al.* at room temperature. Then, using lincomycin (LCM) as a template molecule, molecularly imprinted polymer (MIP) was formed on the surface of Eu-BTC by copolymerization (Fig. 2b). The fluorescent probe based on Eu-BTC coated with MIP was used for the selective determination of LCM. The rough surface of the synthesized Eu-BTC contained smooth rod-like crystals due to the formation of MIP layers on the surface of the Eu-BTC. The probe utilized both Eu-BTC and MIPs, and the recognition site of the probe can be selectively adsorbed by LCM to quench the fluorescence of Eu-BTC. Eu-BTC can also be prepared by 1,2,4-benzene tricarboxylic acid linked with Eu^{3+} ions and the co-precipitation method.[55] The morphology of Eu-BTC changed from a dense spherical shape to an irregular honeycomb shape by adjusting the pH of the reaction solution. With the increase in pH value, the morphology of Eu-BTC changed from a dense spherical shape to an irregular honeycomb shape. The crystal structure and thermal stability of Eu-BTC MOFs were consistent, the luminescence characteristics of Eu-BTC were related to the surface morphology, and the compact spherical structure had stronger emission intensity.

Synthesis of Tb-BTC. Yang *et al.* synthesized the hollow Tb-BTC using a one-pot solvothermal method (Fig. 2f and g).[56] The shape was a hollow sphere with a size of 5 μm, and Tb-BTC can detect Fe^{3+} by the luminescence quenching effect. The method had the advantages of simple operation, mild conditions, high yield, uniform morphology and good stability, and can be used for the determination of trace Fe^{3+}.[57]

Synthesis of other rare earth-BTC. The Nd-BTC was prepared by Asgari *et al.* using a solvothermal method with neodymium nitrate and DMF as the metal precursor and solvent.[59] Surble *et al.* prepared Pr-BTC in deionized water.[60] Pr-BTC consisted of nine-coordinated rare earth polyhedral chains linked by phenyl tricarboxylic acid groups. The chain was composed of square antiprisms with shared sides, and the coordination of rare earth atoms was ensured by oxygen atoms of the carboxylates and a terminal water molecule. Ren *et al.* grafted three different diamines to the coordination instability of Er(III) ions into the channel of the de-solvated Er-BTC.[57] Er-BTC is an effective heterogeneous catalyst for condensation reactions due to its high thermal stability[61] and permanent porosity.[62] Yb-BTC with Yb^{3+} as the metal center and phthalic acid as the ligand was constructed by a solvothermal method.[63] Yb-BTC is a typical microporous material whose high specific surface area and pore structure are conducive to the diffusion of reactant molecules. The unsaturated Yb metal coordination site on the skeleton can serve as the active Lewis acid center.[64]

Rare earth-based MOFs have a variety of remarkable properties, and bimetallic MOFs show synergistic effects and improved performance as compared with similar monometallic materials. MOFs containing bimetals represent the active frontier of heterogeneous catalyst development, which increases the dispersion of the two metals on the carbon composite support. Bimetallic MOFs can be used to create efficient, robust, non-noble metal catalysts to develop sustainable chemical processes. The synergy of the bimetallic centers can have unexpected effects on the effect of the catalyst. Therefore, the MOF of some bimetallic centers containing rare earth elements are described. Kong *et al.* developed the bow-shaped Zr/La bimetallic organic skeleton, which had the adsorption capacity of harmful oxygen anion, and the ratio of Zr to La in Zr/La-BTC influenced the performance.[65] Zr/La-BTC MOFs were prepared by the hydrothermal method, and the mixture of lanthanum nitrate, zirconium nitrate and BTC was dispersed in the DMF solution. In the synthesis of Zr/La-BTC composites, La and Zr were combined to form bow-like products. The ratio of La/Zr played a crucial role in the final structure. The bow-knot morphology disappeared with the increasing of the Zr component, and 0.1 Zr/La-BTC had the best adsorption performance. Foratirad *et al.* prepared tubular and secondary sea urchin-structured bimetal–organic frameworks (ST-MOFs) by cathodic electrodeposition on nickel foam in aqueous samarium nitrate and tellurium nitrate containing organic linkers. A bimetallic lanthanide MOF composed of samarium and thulium elements was directly grown on the surface of nickel foam by a simple electrochemical deposition method.[66] Besides the influence of the ligand and coordination, there are many ways to adjust the catalytic performance of MOFs. The required nanodots can be formed by means of interface etching and precipitation.[67–69]

2.2. ZIF

The structural design of MOFs also gives them great application potential in the fields of gas separation and storage, catalysis, thin films, biomedical imaging, and sensors. As a branch of MOF materials, zeolite imidazole frameworks (ZIFs) are nanoporous materials formed by chemical bonding between Zn^{2+} and Co^{2+} as metal ligands and imidazole, and imidazole and other compounds as organic ligands.[70,71] ZIFs are new porous materials with great application prospects, which combine the advantages of MOFs and zeolites, and possess high specific surface area and structural and functional tunability, as well as high chemical and thermal stability.[72] The excellent characteristics of ZIFs lay a good foundation for their application in catalysis,[73] gas storage and separation[74] and other fields. Therefore, how to improve the application performance of ZIFs has become a hot topic. Ce is one of the most attractive rare earth metals because of its free conversion between Ce(III) and Ce(IV) oxidation states.[75] Cerium-based nanomaterials can jump between the III and IV valence states, causing Ce to play a role in the activation of oxygen in multiphase catalysis, such

as CO oxidation,[76,77] solid oxide fuel cells (SOFCs),[78,79] photocatalytic oxidation,[80,81] soot oxidation,[82,83] *etc.*

Solution method. Inspired by this practical application, Zhao *et al.* dissolved cerium nitrate and zinc nitrate in methanol at the same time, and then added 2-methylimidazole in methanol solution, followed by stirring and washing to prepare Ce-ZIF-8 particles. The final product was obtained after carbonization and acid washing, with Ce sites embedded in graded macro-meso-microporous N-doped carbons (Ce SAS/HPNC). Ce SAS/HPNC with a unique 3D layered and ordered porous structure had small pore sizes and high specific surface area.[83] Chen *et al.* dissolved different contents of rare earth complexes and dimethyl imidazole in deionized water and methanol solution, and added a mixed solution of hexyl trimethyl ammonium bromide and zinc nitrate containing methanol into the system to obtain ZIF-8 particles loaded with rare earth complexes (Ln complex@ZIF-8) by an *in situ* method. The rare earth complexes were loaded into ZIF-8 pores through the electrostatic effect and π–π stacking. A stopper with silane at one end was selectively inserted into the pores of the surface layer of ZIF-8 particles to plug the Ln complex@ZIF-8 surface layer pores.[85] The Zn^{2+} and 2-methylimidazole-formed ZIF-8 are sensitive to a weak acid environment,[86] which helps to release drugs into cancer cells. In addition, Gd has more single electrons in its outermost layer, while Tm^{3+} makes its radiative deexcitation process easier due to its diamagnetization, thus enhancing fluorescence.[87] Based on this, Xu *et al.* dissolved potassium ferricyanide, gadolinium nitrate and thulium chloride in deionized water, respectively, followed by mixing and centrifuging. By adjusting the doping ratio of Gd^{3+} and Tm^{3+}, a series of double rare earth-doped Prussian blue nanoparticles (Gd/TM-Pb) were synthesized. ZIF-8, an acid-responsive metal–organic framework, was then coated on the surface of Gd/TM-Pb, and polydopamine (PDA) was modified on the surface to form a composite nanomaterial (Gd/Tm-Pb@ZIF-8@PDA). The Gd/Tm-Pb@ZIF-8@PDA had photothermal stability and the ability to release drugs due to a pH/glutathione (GSH) dual response.[88] Guo *et al.* prepared La-doped ZIF-8 material with a feed ratio of 3 at% by a solution method, and further prepared La-doped ZnO nanoparticles through a subsequent high-temperature calcination process. La doping was beneficial for obtaining sphere-like nanostructures with smaller particle size,[89] but La doping did not change the crystal structure of ZIF-8 and the derived ZnO nanomaterials.[90]

Vapor phase method. Ce-Doped ZIF-8 was also studied by Wu *et al.* by using a steam phase method to dissolve a certain amount of zinc nitrate and dimethylimidazole in deionized water, followed by filtering and drying the obtained solid ZIF-8 as zinc source precursor, and some of the zinc nitrate was replaced with cerium nitrate (Ce@ZIF-8). The Ce@ZIF-8 sample was obtained by *in situ* doping with different concentrations of Ce.[84]

As a branch of metal–organic framework materials, ZIF-67, with the shape of dodecahedron, is an important organic framework material through which various cobalt-based functional materials can be expanded. ZIF-67 has an open skeleton structure, large specific surface area and regular pore structure, and is widely used in electrochemical energy storage, electrocatalysis, supercapacitors, electroanalytical chemistry, flexible electrodes, and flexible electronic sensing.[91] ZIF-67 has been widely used as a self-sacrificing template to construct hollow porous materials due to its simple synthesis and high specific surface area.[92–94] Rare earth elements have a special 4f shell electron configuration and exhibit special physical and chemical properties. Li *et al.* dispersed 2-methylimidazole, samarium nitrate, and cobalt nitrate in deionized water to prepare Sm-ZIF-67, and then Sm-ZIF-67 was pyrolyzed to obtain N-doped carbon-coated Sm_2O_3-Co nanoparticles. The introduction of Sm_2O_3 improved the electrocatalytic performance of the oxygen reduction reaction (ORR). The synergistic effect between Sm_2O_3 and Co species increased the effective potential, half-wave potential, and limiting current density.[95]

2.3. Other rare earth MOFs

2.3.1 Hydrothermal method

Synthesis of Tb-MOFs. Tb(TCA)(NDC)·H_2O, a Tb-MOF, was prepared by a hydrothermal method using 4,4,4-triphenylamine tricarboxylic acid (H_3TCA) and 2,7-naphthalenedicarboxylic acid (H_2NDC) as ligand.[97] Doping Eu^{3+} in Tb(TCA)(NDC)·H_2O resulted in better optical performance.[98] By using pyrazine-2,3-dicarboxylic acid as the ligand and terbium nitrate as the metal precursor, Tb-MOF was synthesized in a DMF and water mixture solution.[99] Tb-MOFs have the advantages of frequent detection in styrene vapor and as luminescent sensors. With trimesic acid as the ligand and terbium nitrate as the metal precursor, another Tb-MOF was synthesized in ethanol for the detection of volatile organic compounds (VOCs).[100] Physical quantity temperature is an important indicator in industrial production, but it is difficult to measure the temperature of sub-micron objects or fast-moving objects with conventional sensors or thermometers. $[Tb_2(bpydc)_3(H_2O)_3]\cdot n$DMF was the ratiometric luminescence thermometer material. Terbium nitrate, 2,2′-bipyridine-5,5′-dicarboxylic acid and DMF were mixed and stirred at room temperature and sonicated to ensure adequate mixing. Afterwards, the solid was immersed in DMF solution and stirred to remove the unreacted linker, then washed with ethanol by Soxhlet extraction. The unique breathing behavior of $[Tb_2(bpydc)_3(H_2O)_3]\cdot n$DMF is due to a structural transition during formation. The carboxyl groups connected the TbO_x (x = 7 or 8) polyhedral into 1D inorganic chain-like structures, and the bpydc groups joined these chains in series into a 3D backbone structure. 1D channels were solvent accessible when DMF was present in the structure. As the solvent was removed, the 1D channel shrank and the structure transitioned to non-porous, which was an irreversible process.[101] Tb-MOFs can strengthen and quench the ligand central ions to produce many glowing colors for multi-colored luminescent materials. Ou *et al.* added terbium acetate tetrahydrate to DMF and dissolved it by ultrasound to get a terbium salt solution. Homophonic acid was added to DMF to obtain a homophonic acid solution, which was mixed with terbium salt solution to obtain a Tb-MOF powder. Then, the activated carbon

particles were placed in terbium salt solution and immersed in DMF solvent overnight to obtain the Tb-MOF@activated carbon composite. The Eu-MOF material was also obtained by slowly adding all the homoparbenzoic acid solution to the europium salt solution, and the activated carbon particles were placed in the europium salt solution to obtain the Eu-MOF@activated carbon composite. The multifunctional Tb-MOF@activated carbon composite material had high stability and selective adsorption and identification effect on Fe^{3+} and Cr^{3+} heavy metal ions in aqueous solution. The Eu-MOF@activated carbon had a selective adsorption and identification effect on Fe^{3+} heavy metal ions in aqueous solution.[102]

Synthesis of Ho-MOFs. Proton-conductive MOFs have attracted the interest of many scholars with the continuous development of MOFs synthesis techniques. Among them, Ho-MOF can be used as an excellent proton conductive material. Ho-MOF ($[Ho(SIP)(H_2O)_5]\cdot 3H_2O$) was synthesized with holmium as nodes and 5-sulfoisophthalic acid (SIP) as ligands under hydrothermal conditions by the reaction between Ho_2O_3 and NaH_2SIP without any additives.[103] The co-action of abundant water molecules and residual sulfo groups established a staggered pathway for proton conduction.

Synthesis of Tm-MOFs. Tm-MOF ($[Tm(\mu 2\text{-L})\ (\mu 4\text{-L})0.5(H_2O)_2]\ 3H_2O$) was synthesized by a hydrothermal reaction of thulium nitrate with 5-methylpyrazine-2-carboxylic acid. The Pd/Tm-MOF composites were obtained by incorporating small palladium nanoparticles into the Tm-MOF host material by impregnation. Pd/Tm-MOF has a certain catalytic activity in the hydrogenation of styrene. This study shows that metal nanoparticles can be immobilized on MOF materials using uncoordinated carbonyl groups, and the obtained composites can be used for heterogeneous and efficient catalysis.[105] Gd/Tm-MOFs have a great advantage in medical imaging. Thulium chloride, gadolinium chloride, polyvinylpyrrolidone (PVP), and sodium acetate were used to synthesize the rod-like Gd/Tm-MOF crystals in DMF and water.[106] Due to the interdependence of $Gd^{3+}$and Tm^{3+}, Gd/Tm-MOFs have important applications in biochemical engineering. Gd/Tm-MOFs with up-conversion luminescence showed minimal autofluorescence interference, deeper near-infrared (NIR) light penetration, and slight photo-damage for optional imaging and bioassay. When the concentration of the Tm^{3+} was about 6%, the up-conversion luminescence was the strongest, while the gadolinium complexes had advantages in better drug loading and pH-responsive drug release. These special performances were the results influenced by Tm^{3+} and Gd^{3+} mutually.

Synthesis of Lu-MOFs. Lu-MOFs were prepared by the solvothermal method with lutetium as nodes and H_3L as a ligand in DMF solution.[107] The Eu^{3+}/Tb^{3+}@Lu-MOF ratiometric sensor was constructed by introducing Eu^{3+} and Tb^{3+} cations into the Lu-MOF. This sensor can recognize ornidazole and ronidazole with a low detection limit and high quenching efficiency. MOFs-based fluorescence sensing platforms have different effects on different biomarkers, which helps explore the association effects between other biomarkers and MOFs-based sensing platforms.

2.3.2 Solvothermal method

Synthesis of Gd-MOFs. $Gd_2(btec)_2$ was prepared by solvothermal reaction with 1,2,4,5-phenyltetracarboxylic acid (H_4btec), 4,4′-azopyridine and gadolinium nitrate under the conditions of a DMF/H_2O/acetic acid volume ratio of 1 : 1 : 2. The spatial basis of $Gd_2(btec)_2$ is the tri-oblique space group P1, whose asymmetric unit consists of a nine-coordinated Gd center, two half btec nodes, and half a 4,4′-azopyridine. The 4,4′-azopyridine ion is close to a specific location in the Gd_2 $(btec)_2$ channel.[96]

Synthesis of Er-MOFs. The dual-emission ThT@Er-MOF ratiometric fluorescence sensor was a first-synthesis-then-assembly method that introduced the fluorescent dye thioflavin T (ThT) into Er-MOF. Through the synthesis of Er-MOF ($[Er(L)(DMF)_{1.27}]_n$) (H_3L = terphenyl-3,4″,5-tricarboxylic acid) by solvothermal and ultrasonic methods, Alzheimer's disease (AD) biomarkers in cerebrospinal fluid can be detected by ThT@Er-MOF using three methods.[99,104]

Synthesis of Yb-MOFs. 2D Yb-MOFs were prepared with ytterbium as nodes and 4,4′,4″,4‴-(21*H*,23*H*-porphine-5,10,15,20-tetrayl) tetrakis-benzoic acid (H_2TCPP) as the ligand in DMF solution.[101] 2D Yb-MOFs had strong electrochemiluminescence (ECL) behavior because of the larger specific surface area, better electrochemical conductivity and higher productive ratio of fluorescence quantum yield. Ytterbium chloride and $DDPDBCBIm(Br)_2$ ionic liquid can be used to synthetized the Yb-MOFs in DMF solution. The Au nanoparticles were loaded on the Yb-MOFs to obtain the Yb-MOF@Au-NPs nanocomposites for the ultrasensitive detection of the disease-related biomarker carcinoembryonic antigen (CEA).[103]

3 Photocatalysis

In semiconductor photocatalysis, the photogenerated holes and electrons produced by the semiconductors after absorbing light give the semiconductor catalysts photocatalytic properties, effectively avoiding the disadvantages of high temperature, high pressure and cumbersome steps in traditional processes, and this has attracted widespread attention.[108,109] At present, in addition to inorganic materials being used in photocatalysis, organic materials are also being widely reported in the field. The porous structures of MOFs and metal nodes enable the catalyst to act as an island of semiconductor quantum dots.[110,111] Organic structures or light absorption in MOFs can excite these quantum dots.[108,112,113] Rare earth atoms easily gain or lose electrons to enhance charge transfer due to the partial filling of 4f orbital in their electronic structure. Moreover, aqueous solutions of rare earth metal ions are commonly Lewis acids, and most rare earth ions exhibit the trivalent state due to the 4f orbital being unsaturated.[114] Rare earth MOFs also have great advantages in catalyst recycling.

They can be separated from the reaction system by basic operations such as filtration and centrifugation, which is beneficial to the next step of recycling, while some homogeneous catalysts are difficult to recover in the reaction system. Therefore, rare earth MOFs are considered potential photocatalysts.

3.1 Hydrogen evolution reaction

The already reported excellent photocatalysts of MOFs (UiO-66-NH_2 and Ti-MOF-NH_2) have a utilization efficiency of only 5% for sunlight as they only respond to UV light. Therefore, it is necessary to develop catalysts with an excellent response to visible light energy to increase the efficiency of optical utilization.[115]

Recently, some applications for extending photosensitive MOF catalysts have been successively reported.[116,117] MOFs have higher charge mobility compared to inorganic semiconductors, as MOFs can promote the electron diffusion of reactants to disperse them to active sites, thereby improving the catalytic performance of photocatalysts.[118] Therefore, the interaction of metal-linked orbitals is closely related to the choice of inorganic metal junctions.[119,120] The electrons in the 4f orbital of rare earth ions, due to the existence of unpaired electrons, can promote the interaction between the ligand and the cluster charge transfer (LCCT).[121,122] Through the LCCT reaction, rare earth MOFs can limit the recombination of the separated photogenerated electrons and holes.[123–125] Zhang *et al.* chose dye-like azocarboxylic acids as organic linkers to construct a Gd^{3+}-based metal–organic framework $[Gd_2(abtc)(H_2O)_2(OH)_2]_2H_2O$ (Gd-MOF) (H_4abtc = 3,3′,5,5′-azobenzenetetracarboxylic acid), and this Gd-MOF catalyst exhibited a broad absorption band under UV light irradiation. When the Gd-MOF photocatalyst was used, the hydrogen production rate was 7.71 μmol h^{-1}. When the co-catalyst Ag was added in the form of deposition, the catalytic activity was superior. When the Ag deposition amount was 1.5%, the catalytic activity increased by 1.5 times (Fig. 3a and b). In Fig. 3c, compared with Gd-MOF, the addition of Ag presented a lower semicircle at high frequency, and the addition of Ag reduced the charge transfer resistance in the solid-state interface.[126] Yu *et al.* synthesized a MOF of $[Dy_2(abtc)(H_2O)_2(OH)_2]2H_2O$ (H_4abtc = 3,3′,5,5′-azobenzenetetracarboxylic acid), in which the photosensitizer of the MOF is integrated into the MOF through the reaction of Dy^{3+} ions with the dye ligands in the MOF. The absorption edge showed a broad absorption band at 570 nm. The hydrogen evolution rate of Dy-MOF under photocatalysis was 21.53 μmol h^{-1} g^{-1}, and the activity of the catalyst did not decrease after three cycles (in the case of H_2 recovery) (Fig. 3d–f).[127] Wu *et al.* calculated the electronic structure of UiO-66, and explored the electronic structure of the MOF doped with different metal elements, and explained the impact. The low-position nature of the 4f orbital resulted in a negative efficient ligand–metal charge transfer (ELMCT), which enhanced the photocatalytic HER activity of this catalyst, and the UiO-66 node had a stable and efficient LMCT excitation due to the introduction of Ce^{4+}. Furthermore, Ce-MOF has a large and negative LMCT energy, and there is a high photon

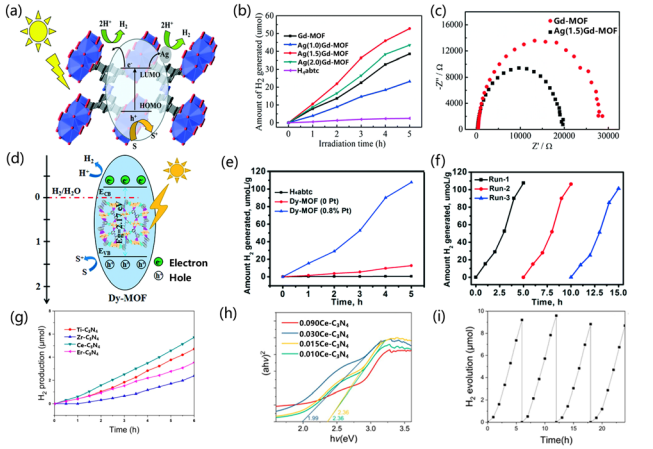

Fig. 3 (a) Schematic diagram of Gd-MOF and Ag/Gd-MOF catalytic hydrogen production reaction under light conditions. (b) Schematic diagram of Gd-MOF structure. (c) EIS Nyquist plots of the prepared electrodes covered with Gd-MOF and Ag(1.5)/Gd-MOF in 0.5 M Na_2SO_4 aqueous solution, Copyright 2016, Royal Society of Chemistry. (d) Schematic diagram of the energy level transitions of Dy-MOF. (e) Hydrogen evolution intensity of a Dy-MOF series. (f) The catalytic activity of Dy-MOF after 15 cycles of visible light irradiation, Copyright 2018, Royal Society of Chemistry. (g) Comparison diagram of metal-C_3N_4 photocatalytic hydrogen evolution intensity. (h) Comparison of Ce–C_3N_4 hydrogen evolution with different doping ratios. (i) 24 hour cycle hydrogen evolution measurement of Ce–C_3N_4 with a doping ratio of 0.015, Copyright 2019, MDPI.

absorption energy in this process, which limits the application of Ce-MOFs as visible light catalysts. The doping of Zr and Ti in UiO-66(Ce) has been studied in detail, and doping with Zr and Ti improved the ELMCT of the catalyst and helped to reduce the adsorption energy, thus improving the photocatalytic properties of Ce-UiO-66.[128] Huang *et al.* synthesized UiO-67, and then used bispyridine of 2,2′-bipyridine-5,5′-dicarboxylic acid (bpydc) to substitute biphenyl-4,4′-dicarboxylic acid (bpdc) and introduced Ce^{4+} ions into UiO-67 to obtain the UiO-67-Ce. UiO-67-Ce can weaken the energy transfer between bpdc and bpydc-Ce, so that the recombination of carriers is suppressed. The LMCT process of UiO-67 was weakened with suppressed carrier recombination. The UiO-67-Ce was ten times more than that of UiO-67, and the HER efficiency of UiO-67-Ce was also better than that of most Zr-based MOF photocatalysts.[129] Zhuang *et al.* synthesized hinge-like CeO_2 by thermally decomposing a Ce-based MOF, and formed a N, S co-doped C-coated structure. Compared with commercial CeO_2, the newly synthesized catalyst has a superior light absorption range because the hinge structures allow light to undergo multiple reflections after being incident. The hinge structure can enhance the charge transfer ability of the porous structure on the C layer, and the low charge transfer resistance in the porous coating, so the catalyst has higher activity in photocatalytic HER and hydrogen production. The modified CeO_2 has a higher mass-normalized velocity than the commercial CeO_2 (555 > 195 μmol h^{-1} g^{-1}).[130] Zhang *et al.* designed a fibrous graphitic carbon nitride(g-C_3N_4) derivative prepared from Ce^{3+}(Ce–C_3N_4)-doped MOFs as a raw material, which can be used as a photocatalyst. The MOF-derived after thermal polymerization

and further heat treatment showed superior photocatalytic activity as compared with Ce–C_3N_4 doped with cerium melamine, benefiting from the fibrous morphology (Fig. 3g and h). Changes in pore structure and larger surface area promote surface charge interactions. The catalytic activity showed that the morphology and structure played a major role in the catalytic performance of the samples. The finer fiber structure provides abundant active sites and therefore has higher photocatalytic activity. Under visible light irradiation, the photocatalytic activity of 0.015 Ce–C_3N_4 went through four cycles within 24 h (Fig. 3i). The researchers further modified the sample with NH_4F to make the fiber morphology of the sample finer and the dispersion better, which further improved the active site and enhanced the absorption of solar energy.[133]

3.2 Carbon dioxide reduction reaction

As a greenhouse gas, the continuous emission of CO_2 leads to global warming. Converting CO_2 into valuable products such as formic acid, ethanol and methane is therefore important to address both environmental and resource concerns. At present, there are many reactions for CO_2 conversion, such as the use of thermal catalysis, photocatalysis and electrocatalysis to convert CO_2 into renewable resources.[131,132,134] For this reason, light-driven CO_2 conversion is currently an effective solution for light energy utilization. In recent decades, more and more materials have been developed and used in the carbon dioxide reduction reaction, such as molecular compounds, semiconductor materials, hybrid materials and so on. In recent years, the ideal capture and conversion concept of photocatalysis has attracted much attention because photocatalysis can promote the absorption of solar energy by materials into usable energy storage. Therefore, the study of efficient catalysts that can react under mild conditions in the photocatalytic process has attracted wide attention. MOFs are ordered porous crystalline materials that use organic ligands to connect metal ions or ion clusters to a network structure. Because of their high porosity, regular pore channels and adjustable pore size, MOFs are promising photocatalysts. The advantages of rare earth MOFs are mainly attributed to the abundant energy level structures of rare earth cations. MOFs with the multi-functional coordination structure of rare earth clusters can provide more possibilities for new rare earth MOFs (Fig. 4a). Rare earth MOFs have strong acid catalytic sites, such as Lewis acid sites, which help to introduce rare earth metals and improve catalytic efficiency (Fig. 4b and c).[135] They also have basic catalytic activity centers from the carefully selected organic ligands.[136] They also have a platform suitable for host-guest interactions in the post-synthesis modification process that helps to produce materials that provide synergistic catalytic performance for specific reactions.[127,137] Rare earth MOFs have the characteristics of enhanced charge transfer mobility[138] and are stable under catalytic conditions, so they can be recycled.[139] Therefore, rare earth MOFs have great research and application potential in the field of photocatalysis.[140] Lee *et al.* found that Eu ions showed good catalytical activity in reductive transformation,[141,142] and Zheng *et al.* used EuRu(phen)$_3$-MOF as a photocatalyst to study

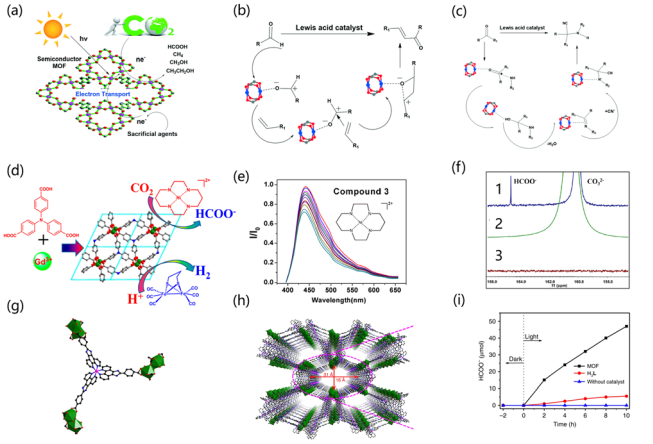

Fig. 4 (a) Scheme of the photochemical CO_2 reduction catalysed by MOFs. (b) Scheme of the Prins reaction catalysed by MOFs. (c) Scheme of the Strecker reaction catalysed by MOFs, Copyright 2017, Royal Society of Chemistry. (d) Construction of Gd-TCA consolidated by the dinuclear units exhibits the opening of the pores along an axis and its application on the light-driven hydrogen production with the Fe–Fe hydrogenase model compound and carbon dioxide reduction with the Ni(Cyclam) complex, respectively. (e) Family of emission spectra of the Gd-TCA suspension (0.02%) upon the addition of complex 3 up to 1.1×10^{-4} M in 1 : 1 CH_3CN/H_2O. (f) ^{13}C NMR spectra for the product obtained from reaction with (1) $^{13}CO_2$ under irradiation; (2)$^{13}CO_2$ in the dark, and (3) $^{12}CO_2$ under irradiation, Copyright 2016, American Chemical Society. (g) Crystal structure of Eu-Ru(phen)$_3$-MOF. (h) Stick/polyhedra model structure of the metalloligand. (i) Time profiles of $HCOO^-$ produced catalytically by Eu-Ru(phen)$_3$-MOF or H_3L, or without catalyst under irradiation with a Xe lamp, Copyright 2018, Springer Nature.

the catalytic reaction of CO_2 reduction to formate.[143] They introduced the Eu cluster as a metal connection node into MOFs, and the resulting independent Eu active cluster sites can be used to reduce CO_2. The EuRu (phen)$_3$-MOF showed the selective photoreduction of CO_2 driven by visible light, and the Eu cluster became the active catalytic center for CO_2 photoreduction after accepting the photoexcited electrons of metal oligomers.[144] Under the irradiation of visible light, Ru(II)(phen)$_3$ was excited into a triplet state, and then an electron was transferred to [Eu(III)–H_2O–Eu(III)] to synthesize [Ru(III)(phen)$_3$]. Therefore, [Eu(III)–H_2O–Eu(III)] achieved the active site [Eu(II)–H_2O–Eu(II)] by accepting two electrons, and CO_2 can be selectively reduced to HCOOH in the dual-electron process.[145] Wu *et al.* reported the research progress on the photocatalytic reduction of CO_2 by Ln-MOF. They used the amino linker (H_3TCA) to synthesize a MOF based on 3D-Gd, which was labeled as Gd-TCA (Fig. 4d). When compound 3 was added to CH_3CN/H_2O (1 : 1), the quenching coefficient K_{SV} of the Gd-TCA suspension was $2.65 \pm 0.2 \times 10^3$ M^{-1}. In the presence of compound 3, the emission band lifetime of Gd-TCA was reduced from 2.38 ns to 1.58 ns. These results confirm the occurrence of photoinduced electron transfer from the Gd-TCA excited state to model compound 3. When Gd-TCA (1 mg) and compound 3 (50 μM) were added to 5 mL CH_3CN/H_2O (1 : 1) solution, the hydrogen evolution efficiency was the highest when the concentration of the sacrificed-electron donor triethylamine was 10.0% (v/v) at

pH = 11.0 (Fig. 4e and f). This MOF was composed of numerous Gd-basic chains that were mainly connected to a network through TCA and stacked through π–π interactions. Gd-TCA is a microporous structure that is suitable for the selective capture of CO_2 and conversion of CO_2. Gd-TCA was deposited on the film of the α-Al_2O_3 plate, which extended the service life of the artificial system, provided a platform for practical application, and made the device easy to operate and recyclable.[146] Wang *et al.* used ligand–metal and metal–ligand charge transfer processes to prepare Eu-MOFs. This activity was due to the high electron transfer in the $Ru(Phen)_3$-based connection network forming a double interpenetrating framework (Fig. 4g and h), which caused a red-shift in the absorption of the photocatalytic MOF system. Combined with the redox process of Eu(III) to Eu(II) and LMCT, the band energy of the MOF system was suitable for CO_2 further reduction, thus activating the C=O of the CO_2 molecule for reduction. After 10 h of illumination, the $HCOO^-$ content was very low in the precursor and without catalyst, and the amount of $HCOO^-$ was about 47 μmol when the catalyst was added, indicating good catalytic performance (Fig. 4i).[143] Zhao *et al.* synthesized Th-MOF by a solvothermal reaction with isonicotinic acid and determined that the adsorption capacity of the MOF of the transition metal thorium (TM-Th MOF) for CO_2 was 42.44 $cm^3\ g^{-1}$. At the same time, this catalyst was an excellent catalyst for CO_2 capture and reduction, mainly attributed to the Lewis acidic sites provided by Th_6 clusters. TM-Th MOF showed catalytic ability for the CO_2 cycloaddition reaction.[147] Zhang *et al.* used PCN-900(Eu) to conduct CO_2 cycloaddition with epoxides. They immersed the synthesized PCN-900(Eu) in DMF solution containing Co^{2+} to prepare CoTCPP-CoBPYDC. The Co of this catalyst can provide acidic sites to promote the conversion of epoxides. The crystalline phase of the MOF was cubic, and the metal sites were located at the vertices, edges and surfaces of the cubic cage, which were highly adjustable, resulting in the high porosity of the MOFs.[148] Zhou *et al.* added a linear linking group to PCN-905-SO_2 to achieve a tandem protection-aldol reaction. It formed large cuboid crystals with open metal sites and low connectivity, making MOF stable in water, and realizing the accurate placement of functional groups in the pore environments to achieve functionalization. They used the rare earth coordinatively unsaturated cluster of PCN-905-SO_2 to place the $BDCSO_3H$ linker with Brønsted acid sites on the rare earth cluster post-synthesis. This MOF combined with NH_2 groups on the main linker of PCN-905-SO_2 can be used as an acid and alkali bifunctional catalyst, but also avoids the neutralization reaction of acid and alkali.[149]

Functional linking groups with excitation and extended lifetimes of excited states can be added to MOFs, enabling the more efficient separation of ligand–metal photogenerated holes and electrons. The energy levels of vacuum alignment can also be adjusted by ligand functionalization However, due to the limited light absorption energy of Ce-UiO-66, it is difficult to absorb visible light. Sun *et al.* tried to modify the ligand and doped with Zr/Ti to improve the negative LMCT energy of Ce-UiO-66 and reduce the absorbed energy. The Ce-UiO-66 (Ti_4)-I had 1.65 eV and 2.5 eV light adsorption energy in the solar radiation range.[114] Cai *et al.* constructed the heterostructure between Ce-MOF and Bi_2MoO_6 by electronic coupling. The structure of Ce-MOF is rod-like, and the structure of BMO is lamellar. The combination of the two gives the material a high surface area and promotes strong contact between them. The Ce-centered MOF was synthesized with benzene tricarboxylic acid as the ligand. The photoreduction performance and adsorption capacity of CO_2 were enhanced by the contact with the electron coupling interface. The products of CO_2 reduction in Ce-MOF/Bi_2MoO_6 composites were CH_4 and CH_3OH. The yields of CH_3OH and HCOOH increased with the increase of heterogeneous components but decreased with the increase of Bi_2MoO_6.[150] Zhang conducted research on rare earth cluster-based organic framework materials for photocatalytic CO_2RR. They assembled the catalytically active rare earth clusters with photosensitive ligands to synthesize the rare earth Eu-Ru$(phen)_3$-MOF catalyst with a macroporous structure and realized the efficient selective conversion of CO_2 to formate, driven by visible light. The photocatalytic reaction rate of formate reached 321.9 μmol h^{-1} mmol MOF^{-1}. The binuclear Eu^{2+} units generated *in situ* under light conditions were the photocatalytic active sites.[143] Our group synthesized a MOF nanosheet structure for photocatalytic CO_2RR.[151] The nanosheet structure has a high specific surface area, the photocatalytic reduction of CO_2 can be carried out efficiently,[151,152] and CO_2 can be efficiently adsorbed on MOF nanosheet structure.[153]

3.3 Other reactions

The design of rare earth MOF photocatalysts can be performed using isometric or building block approaches.[154] This section introduces the reports on the photocatalytic treatment of organic chemicals by rare earth MOFs. Environmental pollutants such as dyes and antibiotics have become an important burden on energy and the environment.[155] Ce has doublet states of excitation and emission from 4f to 5d, which endow it with good energy conservation and no energy loss after the spin state change.[156] Cai *et al.* prepared Ce-doped sensitized Ag_3PO_4 composites by the *in situ* ion exchange deposition method.[157] The crystal structure of MOF was changed due to the addition of Ce. The specific surface area decreased with the increase in Ce but the pore size and pore volume increased to provide more sites for photocatalysis. Ce contains a large number of oxygen vacancies and has a high oxygen storage capacity, which leads to the generation of $^{\bullet}O^{2-}$, and the Ce^{3+}/Ce^{4+} redox pair in the system can promote photogenerated hole transfer to the electron donor (Fig. 5a). Wang *et al.* prepared an isostructural rare earth MOF $[Eu_xTb_{1-x}L(DMF)_2(NO_3)]$ (H_2L = 2,2′-bipyridine-4,4′-dicarboxylic acid) *in situ* by doping a rare earth salt mixture into the Tb-MOF. Under UV irradiation, the degradation efficiency of Tb-MOF to catalyze the decomposition of rhodamine (RhB) was 96%, and that of Eu-MOF was 94% (Fig. 5b).[158] Wu *et al.* used the rigid dicarboxylic acid ligand H_2L as an organic ligand to synthesize Gd-MOF. Its energy band gap (e_g) was 2.68 eV, and it can generate $^{\bullet}OH$ active groups at the same time. In the presence of this catalyst, the decomposition rate of RhB can reach 95%, which greatly improves the decomposition efficiency as compared with the condition without catalyst (15%).[159] Lian *et al.* synthesized a europium-functionalized

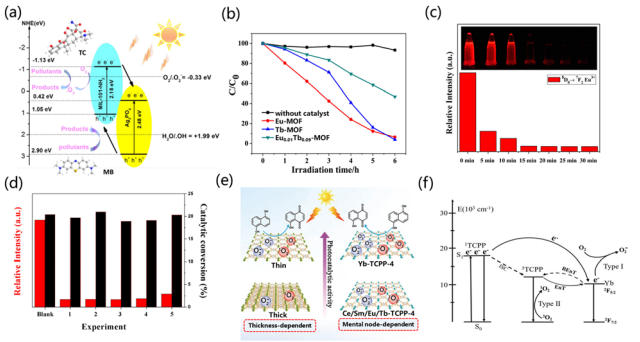

Fig. 5 (a) Schematic of the photodegradation and possible reaction mechanism for the MIL-101-NH_2/Ag_3PO_4 system under visible-light irradiation, Copyright 2020, Elsevier. (b) The photocatalytic degradation profiles of RhB under different conditions, Copyright 2019, Elsevier. (c) $^5D_0 \rightarrow {}^7F_2$ transition intensity ratios from the emission spectra of MIL-125-AM-Eu introduced into α-phenethyl alcohol after UV radiation for different times. (d) Recycling experiments of MIL-125(Ti)-AM-Eu for sensing α-phenethyl alcohol. Red and black columns represent the luminescence intensity of MIL-125(Ti)-AM-Eu and the conversion of the photocatalytic reaction, respectively, Copyright 2016, American Chemical Society. (e) Illustration of the synthesis of 2D Ln-TCPP nanosheets and the thickness- and metal-node-dependent photocatalytic activity. (f) The possible electron and energy transfer paths in 2D Yb-TCPP-4 nanosheets during the photocatalytic process, Copyright 2020, Wiley VCH.

material (MIL-125(Ti)-AM-Eu) based on MIL-125(Ti)-NH_2. The crystals formed by the material were truncated bipyramidal, having a high surface area, good luminescence, high conversion of photocatalytic oxidation of α-acetophenone, and strong selectivity. It had a fluorescence signal reaction to phenyl ethanol. The conversion rate of α-phenethyl alcohol to acetophenone was 20.4% for 6 hours in the presence of catalyst and oxygen (Fig. 5c and d).[160] Jiang *et al.* used a top-down synthesis method to synthesize porphyrin-based lanthanide MOFs without the action of surfactants (Ln-TCPP, TCPP = 4-carboxyphenylporphyrin). Under light conditions, the photocatalytic oxidation of 1,5-dihydroxynaphthalene to juglone by Yb-MOF outperformed other lanthanide MOFs. The possible reason is that the electron transfer between TCPP and Yb^{3+} ions can cause MOF to generate $^{\bullet}O^{2-}$ and O_2, thus showing higher photocatalytic activity (Fig. 5e and f).[161] Kaur *et al.* designed and synthesized Eu-MOF with CdTe-conjugated quantum dots (QDs). The rhodamine 6G dye can be completely degraded by QD/Eu-MOF within 50 min (Fig. 6a).[162] Pan *et al.* reported that chalcone dicarboxylic acid ligands combined with rare earth elements to form MOFs, and reacted the ligand with lanthanide metals to generate seven kinds of rare earth MOFs.[163] Aguirre-Díaz *et al.* prepared a series of rare earth coordination polymers by solvothermal synthesis (RPF-30-Er, RPF-31-Ln (Ln = La, Nd, and Sm)). The photocatalytic conversion rates of the five MOF materials were 60–76% on the oxidative coupling of benzylamine and imine, and the selectivity exceeded 99% (Fig. 6b).[164] Jiang *et al.* constructed porphyrin-based 2D MB-/Yb-TPCC-SO_4 nanosheets. Such rare earth MOFs had the following characteristics (Fig. 6f). The chromophores of MOFs were close to each other but not in contact; the chromophores were highly ordered. 2D MOFs have a larger specific surface area and more accessible active sites, providing abundant active sites and a higher mass transfer rate for improving photocatalytic performance. These unique properties not only facilitate photon capture, energy transfer, and the increase of active centers but also inhibit the quenching of chromophores. In the photocatalytic synthesis of artemisinin on 2D MB-/Yb-TCPP-SO_4 nanosheets, the internal conversion rate of artemisinin was 99%, and the yield was 80% for 3 hours.[165]

In degrading water pollution into less toxic organics, the advanced oxidation process (AOP) of hydrogen peroxide (H_2O_2) has been widely used due to its stronger photocatalytic performance than multifunctional organics.[166–169] AOP not only has the characteristics of high efficiency and easy handling but it can also generate highly active substances *in situ*. Therefore, synthesizing new MOF photocatalysts and participating in the degradation of AOPs of H_2O_2 is a very promising research direction. Xia *et al.* used anthracene dicarboxylic acid as a ligand to prepare a series of lanthanide MOFs by thermal synthesis. In the presence of H_2O_2, about 99% of RhB in solution was degraded by Ce-MOF after 12 min of light irradiation. The efficiency of Dy-MOF to degrade RhB reached 95% at 60 minutes, and the degradation of RhB reached 90% at 60 minutes on Tb-MOFs (Fig. 6c). Ln-MOFs can enhance the photocatalytic performance by rapidly generating hydroxyl radical active species. Because H_2O_2 can produce hydroxyl radicals under light conditions, it is beneficial to the photocatalytic degradation of RhB by lanthanide MOFs (Fig. 6d and e).[170]

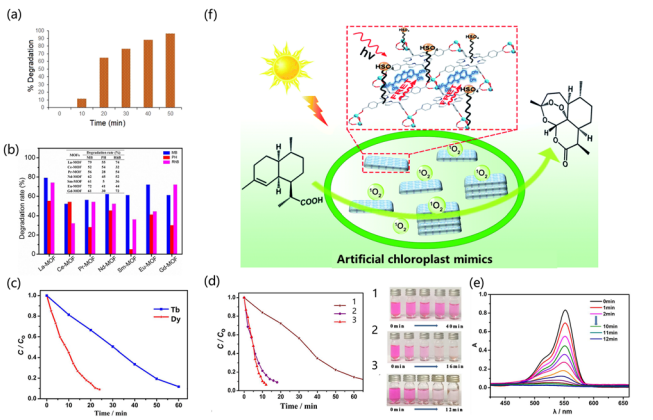

Fig. 6 (a) Changes in the efficiency of the Rh 6G (concentration: 1 mg L^{-1}) samples with irradiation time after photodegradation with 5 mg L^{-1} of QD/Eu-MOF, Copyright 2016, Elsevier. (b) Degradation rates of the MB, PH and RhB solutions in the presence of Ln–MOFs, Copyright 2018, American Chemical Society. (c) RhB degradation by NNU-15(Tb) and NNU-15(Dy) over a H_2O_2/Ln-MOF/RhB system. (d) Photocatalytic reactions at different premixing processes, (Curve 1) premixed NNU-15(Ce)/RhB, (Curve 2) premixed NNU-15(Ce)/H_2O_2, (Curve 3) premixed NNU-15(Ce)/H_2O_2/RhB, (1) Premixed NNU-15(Ce)/RhB, (2) premixed NNU-15(Ce)/H_2O_2, (3) premixed NNU-15(Ce)/H_2O_2/RhB. (e) Time-dependent absorption for the system of NNU-15(Ce)/H_2O_2/RhB/visible light. For all reactions: NNU-15(Ce), 30 mg; H_2O_2, 0.6 M, Copyright 2017, American Chemical Society. (f) Working principle of the constructed 2D ALHS with chloroplast bionic structure for artemisinin production, Copyright 2021, Royal Society of Chemistry.

Aguirre-Díaz *et al.* synthesized five rare earth catalysts, and 1D rare earth-based coordination polymers (CPs) were used as the photocatalyst for the oxidative coupling of amines. Five spirobifluorene-containing Ln-CPs, namely, $[Er_3(Hsfdc)_3(sfdc)_3(H_2O)]\cdot xH_2O$ (RPF-30-Er), $[Ln(Hsfdc)(sfdc)(EtOH)]\cdot S$(RPF-31-Ln, where Ln= La, Nd, and Sm and S = H_2O or EtOH), and $[Ho(Hsfdc)(sfdc)(H_2O)]$ (RPF-32-Ho) (RPF = rare-earth polymeric framework and H_2sfdc = 9,9′-spirobi[9*H*-fluorene]-2,2′-dicarboxylic acid), have been solvothermally synthesized for the oxidative coupling of amine. The selectivity of the oxidative coupling of amine can reach 92% and the conversion rate can reach 60% at the optimal ratio.[171] Zhang *et al.* used the defection-induced nanomanufacturing strategy to prepare the nanostructured MOF-76(Ce)$\{[Ce(BTC)(H_2O)] \times DMF\}_n$ for nitrogen reduction. The nitrogen was adsorbed and desorbed on the MOF catalyst surface by bubbling into the solution. The formation of NH_3 was catalyzed by the strong light, and the production rate of NH_4^+ was 36.4 μmol g^{-1} h^{-1}.[172]

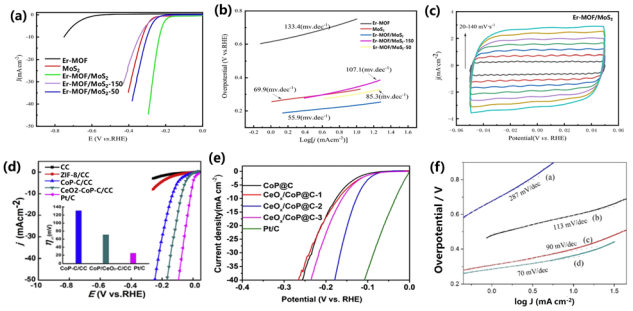

Fig. 7 (a) Linear sweep voltammograms of Er-MOF/MoS_2, MoS_2, and Er-MOF, in 0.5 M H_2SO_4 at a scan rate of 5 mV s^{-1}. (b) The corresponding Tafel plots of Er-MOF/MoS_2, MoS_2. (c) Cyclic voltammetry of Er-MOF/MoS_2 in the non-Faraday potential region at different scanning rates in 0.5 M H_2SO_4, Copyright 2022, Elsevier. (d) Polarization curves of carbon cloth (CC), ZIF-8/CC, CoP-C/CC, CeO_2-CoP-C/CC, and Pt/C in a N_2-saturated 0.5 M H_2SO_4 solution. Scan rate: 2 mV s^{-1}. Inset shows the corresponding overpotential of CoP-C/CC, CeO_2-CoP-C/CC, and Pt/C at the current density of 10 mV cm^{-2} (η_{10}), Copyright 2018, Elsevier. (e) Polarization curves of HER, Copyright 2021, Wiley VCH. (f) The corresponding Tafel plots of different catalysts for HER, Copyright 2021, Wiley VCH.

4. Electrocatalysis

Due to the unique pore structure of the MOF, it can provide more active sites for the catalyst to attach and provide a conductive medium for electron transport.[173] By synthesizing different configurations of MOF materials and embedding multifunctional groups on organic ligands, the catalytic activity can be improved without changing the topology of MOFs. Rare earth elements are very active metals with excellent electronic structures.[174–177] Doping with rare earth elements can change the performance of electrochemical catalysts.[178,179] Their electronic structures, including metals and non-metals, endow them with enhanced HER, OER, CO_2RR, *etc.* properties because of the unique properties of 4f electrons.

4.1 Hydrogen evolution reaction

Hydrogen is a form of clean energy with a high calorific value[180–183] and therefore, hydrogen may become an important energy source on the world energy stage in the foreseeable future. The technologies for the fetching, storage, transportation and application of hydrogen have received extensive attention.[184,185] Hydrogen production by the electrolysis of water has been the mainstream industrial hydrogen production technology since 1789.[186] However, the large overpotential and low electrochemical energy conversion efficiency involved in the hydrogen evolution reaction process have become the main obstacles.[187] Liao *et al.* synthesized the erbium-based MOF material with 1,3,5-benzenetricarboxylic acid as the ligand by the hydrothermal method. Er-MOF/MoS_2 was obtained by doping MoS into MOF material by adjusting the pH. There are a large number of folds on the surface of MoS_2, which are conducive to the exposure of catalytic active sites. Er-MOF/MoS_2 has many micropores that can transport electrolytes to the catalytic surface and improve hydrogen production efficiency. The overpotential of Er-MOF was 790 mV at 10 mA cm^{-2} and that of MoS was 327 mV. It can be seen from Fig. 7a and b that the Tafel slope of Er-MOF/MoS_2 is lower than that of pure MoS_2 and pure Er-MOF. The improved catalyst activity is due to the rough surface formed by the lamellar structure between the MoS_2 and Er-MOF interfaces, which increases the area where the active sites can attach. The pore structure of MOF can reduce the gas-solid surface tension and increase the reaction rate. Er-MOF/MoS_2 and CV curves of MoS_2 are shown in Fig. 7c. Er-MOF/MoS_2 has a high current density and area. The REDOX peak of Er-MOF/MoS_2 is higher than that of MoS_2 under the same conditions. The higher the active surface area, the higher the catalytic activity.[188] Xiong *et al.* used ZIF-8 as a template to synthesize a ternary hybrid CeO_2–CoP–C catalyst by a high-temperature carbonization and low-temperature phosphating route. The carbonization of MOF not only increased the porosity of the catalyst, but the carbon skeleton could also achieve rapid electron transport and efficient mass transfer, which improved the stability of the catalyst. The co-ion exchange of Ce ions effectively doped the rare earth element into the MOF material. The rare earth catalyst has an overpotential of 71 mV at 10 mA cm^{-2} (Fig. 7d).[189] Lan *et al.* reported a CeO_x-modified CoP@carbon material. Since rare earth metals changed the electronic structure of MOF, the HER overpotential was measured to be 127 mV (Fig. 7e).[190] Xue *et al.* reported a Cu_2MoS_4 nanosheet material grown vertically on Ce-MOF, exposing more active sites at the edges. When the HER was measured at a current density of 10 mA cm^{-2}, the overpotential was 350 mV, and the Tafel slope was 70 mV dec^{-1} (Fig. 7f).[173]

4.2 Oxygen evolution reaction

Zhang *et al.* reported a cobalt-doped mixed lanthanum oxide and hydroxide heterostructure using La-MOF-NH_2. As an OER catalyst, the overpotential was 330 mV at a current density of 10 mA cm^{-2} (Fig. 8a).[191] Ma *et al.* reported a Fe-MOF doped with Dy ($Dy_{0.05}$Fe-MOF) by a one-step solvothermal reaction. The results showed that the catalyst was hydrangea shaped and

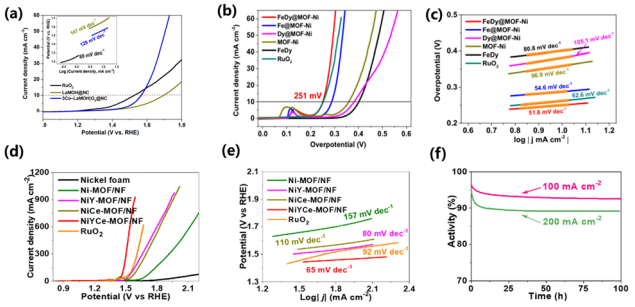

Fig. 8 (a) Polarization curves of RuO_2, LaMOH@NC, and 3Co–LaMO-H|OV@NC in 0.1 M KOH, 10 mV s^{-1} (inset: the corresponding Tafel plots), Copyright 2021, Elsevier. (b) OER performance of the different catalysts in 1.0 M KOH. (c) LSV curves obtained at a scan rate of 5 mV s^{-1}, Copyright 2020, Elsevier. (d) Polarization curves. (e) Corresponding Tafel slopes of different samples for the OER. (f) Long-term testing of NiYCe-MOF/NF for 100 h at different current densities, Copyright 2022, American Chemical Society.

composed of ultrathin nanosheets. The catalyst showed durability, activity, stability and constitutive OER activity. $Dy_{0.05}$Fe-MOF needs an overpotential of 319 mV to drive the OER at a current density of 500 mA cm^{-2}, while Fe-MOF can only drive a current density of 100 mA cm^{-2} under the same overpotential. The less electronegative Dy doping can provide electrons to neighbouring Fe atoms as compared to Fe doping. The Dy and Ni spin ferromagnetic coupling can change the roughness of the substrate surface of the catalyst.[192] Wan *et al.* reported a 3D rhombus nanostructure doped with Fe and Dy by MOF-Ni on carbon cloth. The FeDy@MOF-Ni catalyst required an overpotential of 251 mV to reach 10 mA cm^{-2} and had a Tafel slope of 52.1 mV dec^{-1}. The unique 3D diamond structure and Fe–Dy–Ni coupling synergism gave it electrocatalytic performance (Fig. 8b and c).[193] Li *et al.* reported a MOF nanosheet doped with Y and Ce, which can be applied in the OER. The incorporation of Y and Ce atoms into Ni-MOF resulted in a bimetallic synergistic effect and the construction of rich active centers, thus improving the overall water decomposition performance of the material. At the same time, Y and Ce doping can control the electronic structure of NiYCe-MOF. For the OER, the overpotential at 10 mA cm^{-2} was 245 mV, and the Tafel slope was 65 mV dec^{-1}, but for the HER, the overpotential at 10 mA cm^{-2} was 136 mV. When NiYCe-MOF served as the anode and cathode electrocatalyst at the same time, a voltage of 1.54 V was needed when it reached 100 mA cm^{-2} (Fig. 8d–f).[194] During the OER process, the surface of the MOF catalyst is reconstructed, in which metal oxides and hydroxides are the most common active sites. Most metal elements and metal oxides are thermodynamically stable endpoints of most chemical processes under a strong oxidizing environment. The adjustment and termination of the reforming process are key points in improving the catalytic efficiency.

4.3 Carbon dioxide reduction reaction

The carbon dioxide reduction reaction (CO_2RR) is a very complex reaction process that involves a variety of products, reaction mechanisms, catalysts and electrolytic conditions.[195,196] The CO_2RR also has multiple reaction steps and intermediates, which mainly involve 2, 4, 6, 8 and 12-electron transfers.[197] The CO_2RR is the reason for the product diversity and can convert CO_2 into at least 16 different products through different reaction pathways.[198]

These products can be divided into C1 and C2. The main representative products in C1 are carbon monoxide (CO), acid (HCOOH), methanol (CH_3OH), formaldehyde (HCHO) and methane (CH_4), and the main representative products in C2 are ethylene (CH_2CH_2), ethanol (C_2H_5OH) and acetic acid (CH_3COOH).[199] CO and HCOOH in C1 are the most efficient products in the CO_2RR.[200] The process of C1 production from CO_2RR is relatively simple, including CO_2 adsorption, intermediate formation and product desorption. In contrast, the mechanism by which CO_2RR generates multi-C products is a complex process involving multiple electrochemical and chemical reactions. C2 is more difficult to produce than C1 because C2 is a multi-carbon product that has to transfer more electrons and protons.[201] For example, it takes 12 electrons to convert carbon dioxide into ethylene, and 2 electrons to produce carbon monoxide. In general, C2 and C3 multi-C products are more attractive than C1, but they also suffer from low selectivity, high energy consumption, and complex reactions. In the process of the CO_2RR, the change in the C=O bond is a necessary step; however, CO_2 with the C=O bond is very stable, and the destruction of the C=O bond requires a dissociation energy of about 750 kJ mol^{-1}.[202] Therefore, the CO_2RR requires higher energy. Rare earth MOFs are very important in the CO_2RR process to reduce energy loss. In the process of CO_2RR reaction, the C=O bond of CO_2 will coordinate with the core elements of the rare earth MOF catalyst, reducing the bond energy of C and O atoms, weakening the stability of the CO_2 molecular structure, thus reducing the energy barrier of the CO_2 molecular fracture reaction, and eventually catalyzing the whole CO_2RR process. Luna *et al.* studied the growth of MOF films on high-curvature gold nanostructured microelectrodes (AuNMEs). The porosity and crystal structure of MOF films are easy to change. Re-ndc-fcu-MOF (Re = Y, ndc = 1,4-naphthalenedicarboxylic acid, fcu = face-centered cubic) thin films grown on AuNME were prepared by solvothermal deposition, and the size of the Re-ndc-fcu-MOF octahedral crystal was 50 μm. For the CO_2RR electrocatalyst, the Faraday efficiency of CO was 18%. Because Re-ndc-fcu-MOF did not completely coat the nanoneedles, many exposed active sites of AuNME could contribute to CO formation (Fig. 9a–c). The adsorption capacity and Lewis acidity of catalysts can be changed by adjusting the type of organic ligands or metal junctions.[203] Nam *et al.* used UiO-66 as the starting material, and changed the organic ligand of UiO-66 to NH_2BDC to enhance the adsorption capacity of CO_2 because the amino group can provide a stronger force with CO_2. The effect of acidity on CO_2RR was explored by replacing the central cluster from Zr to Y (Fig. 9d and e). At the same time, the active substance Ag nanoparticles were added to improve the selectivity, and the addition of Ag nanoparticles increased the local CO_2 concentration, which led to the

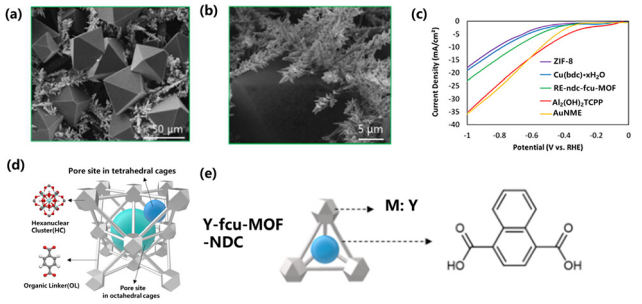

Fig. 9 SEM images of RE-ndc-fcu-MOF on AuNME before (a) and after electrochemical reaction (b). (c) Linear sweep voltammetry (LSV) scans (0 to −1 V *vs.* RHE, 0.1 M $KHCO_3$) of different MOF@AuNMEs and AuNME control, Copyright 2018, American Chemical Society. (d) Microscopic diagram of fcu-MOF-BDC. (e) The metal node of MOF is replaced with Y to get Y-fcu-MOF-BDC, Copyright 2020, American Chemical Society.

enhancement of CO_2RR and inhibited the HER. The Faraday efficiency of CO was 60% at a current density of 30 mA cm^{-2}.[204]

5. Conclusion and prospects

In the past 30 years, MOFs have fascinated researchers with their structural diversity and tunability. Various MOFs have been synthesized from elements with metallic nodes, including elements in the s-, p-, d-, and f-regions. However, different types of MOFs have nearly similar functions, and MOFs synthesized by rare earth elements including scandium, yttrium and lanthanide have similar structures and functions to form an interesting series. Rare-earth MOFs can possess properties common to many MOF families, and they also display unique structures and properties due to the unique 4f electron shells of rare-earth elements. We have reviewed the progress of rare earth MOFs, including the synthesis of rare earth polymetallic MOFs materials, their structures, and current developments in the use of rare earth polymetallic MOFs in photo/electrocatalysis applications. Although there is much research on rare earth MOFs materials, the design of rare earth MOFs still needs to be improved, and the applications of MOFs still have great research potential (Fig. 10) For example, there is still no effective means of controlling the formation of tetranuclear, hexanuclear and nonanuclear cluster nodes, and there are many more cases where two or more clusters are in a network topology, which presents certain challenges. To improve the electrocatalysis properties of rare earth MOFs, the nuclear stability of MOFs is still a problem that needs to be solved. To improve the photocatalysis properties of rare earth MOFs, the problem to be overcome is to find multifunctional MOFs that have both photooxidation and photoreduction capabilities. To achieve the above goals, it is also necessary to find a substance that can span the energy bands of photocatalytic oxidation and reduction, while complying with the laws of thermodynamics. At the same time, in the narrow band gap structure, it can respond sensitively to light. Therefore, the topological structure of rare earth MOFs is correlated with photocatalytic performance. In the study of Re-MOF, MOF materials can not only complete conventional photocatalysis, electrocatalysis and other aspects but can also be used as materials for the development of battery electrodes to improve the working efficiency of batteries.[205–208] If the above challenges are overcome, rare-earth MOFs will have broader prospects and development in other fields. There are numerous unknown areas that need to be explored in the future.

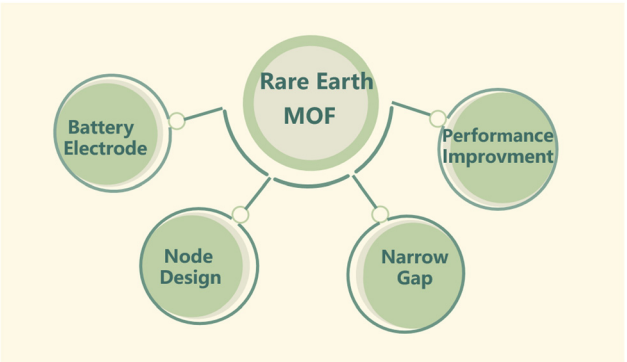

Fig. 10 Schematic diagram showing the prospect of rare earth MOF.

Conflicts of interest

There are no conflicts to declare.

Acknowledgements

We gratefully acknowledge the financial support from the National Nature Science Foundation of China (Grant No. 22122113) and National Key R&D Program of China (Grant No. 2022YFB3506200).

Notes and references

1 M. Kondo, T. Yoshitomi, H. Matsuzaka, S. Kitagawa and K. Seki, Three-dimensional framework with channeling cavities for small molecules: $\{[M_2(4,4\text{-bpy})_3(NO_3)_4]\cdot xH_2O\}_n$(M = Co, Ni, Zn), *Angew. Chem., Int. Ed. Engl.*, 1997, **36**, 1725–1727.

2 A. K. Cheetham, G. Férey and T. Loiseau, Open-framework inorganic materials, *Angew. Chem., Int. Ed.*, 1999, **38**, 3268–3292.

3 H. Furukawa, K. E. Cordova, M. O. Keeffe and O. M. Yaghi, The chemistry and applications of metal–organic frameworks, *Science*, 2013, **341**, 1230444.

4 S. R. Batten, N. R. Champness, X. Chen, J. Garcia-Martinez, S. Kitagawa, L. Öhrström, M. O'Keeffe, M. P. Suh and J. Reedijk, Coordination polymers, metal–organic frameworks and the need for terminology guidelines, *CrystEngComm*, 2012, **14**, 3001–3004.

5 S. R. Batten, N. R. Champness, X. Chen, J. Garcia-Martinez, S. Kitagawa, L. Öhrström, M. O. Keeffe, M. Paik Suh and J. Reedijk, Terminology of metal–organic frameworks and

coordination polymers, *Pure Appl. Chem.*, 2013, **85**, 1715–1724.
6 O. M. Yaghi, M. O'Keeffe, N. W. Ockwig, H. K. Chae, M. Eddaoudi and J. Kim, Reticular synthesis and the design of new materials, *Nature*, 2003, **423**, 705–714.
7 O. M. Yaghi, Reticular chemistry-construction, properties, and precision reactions of frameworks, *J. Am. Chem. Soc.*, 2016, **138**, 15507–15509.
8 Z. Chen, P. Li, R. Anderson, X. Wang, X. Zhang, L. Robison, L. R. Redfern, S. Moribe, T. Islamoglu, D. A. Gomez-Gualdron, T. Yildirim, J. F. Stoddart and O. K. Farha, Balancing volumetric and gravimetric uptake in highly porous materials for clean energy, *Science*, 2020, **368**, 297–303.
9 P. Li, N. A. Vermeulen, C. D. Malliakas, D. A. Gómez-Gualdrón, A. J. Howarth, B. L. Mehdi, A. Dohnalkova, N. D. Browning, M. O. Keeffe and O. K. Farha, Bottom-up construction of a superstructure in a porous uranium-organic crystal, *Science*, 2017, **356**, 624–627.
10 C. Liu, D. Zhang and D. Zhu, In situ hydrothermal decarboxylation for unprecedented three-dimensional lanthanide–organic frameworks, *Inorg. Chem. Commun.*, 2008, **11**, 903–906.
11 W. Mao, L. Xiang and Y. Chen, Rare-earth metal complexes of β-diketiminato ligands bearing pendant nitrogen or oxygen donors, *Coord. Chem. Rev.*, 2017, **346**, 77–90.
12 M. J. Vitorino, T. Devic, M. Tromp, G. R. Fã Rey and M. Visseaux, lanthanide metal–organic frameworks as Ziegler-Natta catalysts for the selective polymerization of isoprene, *Macromol. Chem. Phys.*, 2009, **210**, 1923–1932.
13 S. Ma and H. Zhou, A metal–organic framework with entatic metal centers exhibiting high gas adsorption affinity, *J. Am. Chem. Soc.*, 2006, **128**, 11734–11735.
14 D. Xue, Y. Belmabkhout, O. Shekhah, H. Jiang, K. Adil, A. J. Cairns and M. Eddaoudi, Tunable rare earth-fcu-MOF platform: access to adsorption kinetics driven gas/vapor separations via pore size contraction, *J. Am. Chem. Soc.*, 2015, **137**, 5034–5040.
15 K. Otake, Y. Cui, C. T. Buru, Z. Li, J. T. Hupp and O. K. Farha, Single-atom-based vanadium oxide catalysts supported on metal–organic frameworks: selective alcohol oxidation and structure–activity relationship, *J. Am. Chem. Soc.*, 2018, **140**, 8652–8656.
16 J. Lee, O. K. Farha, J. Roberts, K. A. Scheidt, S. T. Nguyen and J. T. Hupp, Metal–organic framework materials as catalysts, *Chem. Soc. Rev.*, 2009, **38**, 1450–1459.
17 Y. Qian, F. Zhang and H. Pang, A review of MOFs and their composites-based photocatalysts: synthesis and applications, *Adv. Funct. Mater.*, 2021, **31**, 2104231.
18 F. Guo, S. Yang, Y. Liu, P. Wang, J. Huang and W. Sun, Size engineering of metal–organic framework MIL-101(Cr)–Ag hybrids for photocatalytic CO_2 reduction, *ACS Catal.*, 2019, **9**, 8464–8470.
19 L. Zhang, X. Shi, Z. Zhang, R. P. Kuchel, R. Namivandi-Zangeneh, N. Corrigan, K. Jung, K. Liang and C. Boyer, Porphyrinic zirconium metal–organic frameworks (MOFs) as heterogeneous photocatalysts for PET-RAFT polymerization and stereolithography, *Angew. Chem., Int. Ed.*, 2021, **60**, 5489–5496.
20 B. Han, X. Ou, Z. Deng, Y. Song, C. Tian, H. Deng, Y. Xu and Z. Lin, Nickel metal–organic framework monolayers for photoreduction of diluted CO_2: metal-node-dependent activity and selectivity, *Angew. Chem., Int. Ed.*, 2018, **57**, 16811–16815.
21 S. Payra and S. Roy, From trash to treasure: probing cycloaddition and photocatalytic reduction of CO_2 over cerium-based metal–organic frameworks, *J. Phys. Chem. C*, 2021, **125**, 8497–8507.
22 X. Li, X. Yang, H. Xue, H. Pang and Q. Xu, Metal–organic frameworks as a platform for clean energy applications, *EnergyChem*, 2020, **2**, 100027.
23 H. Huang, Y. Zhao, Y. Bai, F. Li, Y. Zhang and Y. Chen, Conductive metal–organic frameworks with extra metallic sites as an efficient electrocatalyst for the hydrogen evolution reaction, *Adv. Sci.*, 2020, **7**, 2000012.
24 D. Li, H. Xu, L. Jiao and H. Jiang, Metal–organic frameworks for catalysis: state of the art, challenges, and opportunities, *EnergyChem*, 2019, **1**, 100005.
25 S. Chinnapaiyan, U. Rajaji, S. Chen, T. Liu, J. I. de Oliveira Filho and Y. Chang, Fabrication of thulium metal–organic frameworks based smartphone sensor towards arsenical feed additive drug detection: applicable in food safety analysis, *Electrochim. Acta*, 2022, **401**, 139487.
26 M. Wang, Y. Tang and Y. Jin, Modulating catalytic performance of metal–organic framework composites by localized surface plasmon resonance, *ACS Catal.*, 2019, **9**, 11502–11514.
27 P. Mazierski, A. Mikolajczyk, B. Bajorowicz, A. Malankowska, A. Zaleska-Medynska and J. Nadolna, The role of lanthanides in TiO_2-based photocatalysis: a review, *Appl. Catal., B*, 2018, **233**, 301–317.
28 P. Parnicka, W. Lisowski, T. Klimczuk, J. łuczak, A. Żak and A. Zaleska-Medynska, Visible-light-driven lanthanide–organic-frameworks modified TiO_2 photocatalysts utilizing up-conversion effect, *Appl. Catal., B*, 2021, **291**, 120056.
29 Y. Zhang, H. Chen, Y. Pan, X. Zeng, X. Jiang, Z. Long and X. Hou, Cerium-based UiO-66 metal–organic frameworks explored as efficient redox catalysts: titanium incorporation and generation of abundant oxygen vacancies, *Chem. Commun.*, 2019, **55**, 13959–13962.
30 P. Mahata, K. V. Ramya and S. Natarajan, Pillaring of $CdCl_2$ like layers in lanthanide metal–organic frameworks: synthesis, structure, and photophysical properties, *Chem. – Eur. J.*, 2008, **14**, 5839–5850.
31 Y. Liu, D. Huang, M. Cheng, Z. Liu, C. Lai, C. Zhang, C. Zhou, W. Xiong, L. Qin, B. Shao and Q. Liang, Metal sulfide/MOF-based composites as visible-light-driven photocatalysts for enhanced hydrogen production from water splitting, *Coord. Chem. Rev.*, 2020, **409**, 213220.
32 P. S. Abraira, S. M. F. Vilela, A. A. Babaryk, M. C. Antonino, P. Gregorio, F. Salles, S. Navalón, H. García and P. Horcajada, Nickel phosphonate MOF as efficient water splitting photocatalyst, *Nano Res.*, 2021, **14**, 450–457.

33 G. Blasse and B. C. Grabmaier, *Luminescent materials*, *Springer*, *Berlin*, 1994.
34 B. D. Chandler, D. T. Cramb and G. K. H. Shimizu, Microporous metal–organic frameworks formed in a stepwise manner from luminescent building blocks, *J. Am. Chem. Soc.*, 2006, **128**, 10403–10412.
35 P. R. Selvin, The renaissance of fluorescence resonance energy transfer, *Nat. Struct. Mol. Biol.*, 2000, **7**, 730–734.
36 S. J. Shah, W. Li, Y. Tang, Y. Hu, S. Jiang, H. He, R. Wang, Z. Zhao and Z. Zhao, Ligand-sharing growth of upconversion UCNP($NaYbF_4$:Tm^{3+})/NMIL(Ti) nanohybrids with extended light absorbance for acetaldehyde photodegradation under high humidity, *Appl. Catal., B*, 2022, **315**, 121555.
37 W. Chen, L. Li, X. Li, L. Lin, G. Wang, Z. Zhang, L. Li and Y. Yu, Layered rare earth-organic framework as highly efficient luminescent matrix: the crystal structure, optical spectroscopy, electronic transition, and luminescent sensing properties, *Cryst. Growth Des.*, 2019, **19**, 4754–4764.
38 H. Tong, Y. Ji, T. He, R. He, M. Chen, J. Zeng and D. Wu, Preparation and photocatalytic performance of UIO-66/La-MOF composite, *Water Sci. Technol.*, 2022, **86**, 95–109.
39 S. K. Das, S. Chatterjee, S. Bhunia, A. Mondal, P. Mitra, V. Kumari, A. Pradhan and A. Bhaumik, A new strongly paramagnetic cerium-containing microporous MOF for CO_2 fixation under ambient conditions, *Dalton Trans.*, 2017, **46**, 13783–13792.
40 S. Dong, L. Peng, W. Wei and T. Huang, Three MOF-templated carbon nanocomposites for potential platforms of enzyme immobilization with improved electrochemical performance, *ACS Appl. Mater. Inter.*, 2018, **10**, 14665–14672.
41 P. A. Julien, C. Mottillo and T. Friš I, Metal–organic frameworks meet scalable and sustainable synthesis, green chemistry: an international journal and green chemistry resource, *Green Chem.*, 2017, **19**, 2729–2747.
42 M. Campanelli, T. Del Giacco, F. De Angelis, E. Mosconi, M. Taddei, F. Marmottini, R. D. Amato and F. Costantino, Solvent-free synthetic route for Cerium(IV) metal–organic frameworks with UiO-66 architecture and their photocatalytic applications, *ACS Appl. Mater. Inter.*, 2019, **11**, 45031–45037.
43 S. M. Prabhu, S. Imamura and K. Sasaki, Mono-, Di-, and Tricarboxylic Acid Facilitated Lanthanum-Based Organic Frameworks: Insights into the Structural Stability and Mechanistic Approach for Superior Adsorption of Arsenate from Water, *ACS Sustainable Chem. Eng.*, 2019, **7**, 6917–6928.
44 A. Jeyaseelan and N. Viswanathan, Facile synthesis of tunable rare earth-based metal organic frameworks for enhanced fluoride retention, *J. Mol. Liq.*, 2021, **326**, 115163.
45 H. Zhang, J. Qiu, M. Xing, X. Liu, X. Ma, L. Ouyang, Y. Qiao, W. Qian and X. Liu, Hydrogen plasma treated-Ce–BTC nanorods enable enhanced antibacterial activity and soft tissue sealing ability, *Chem. Eng. J.*, 2022, **449**, 137881.
46 M. M. Peng, M. Ganesh, R. Vinodh, M. Palanichamy and H. T. Jang, Solvent free oxidation of ethylbenzene over Ce–BTC MOF, *Arab. J. Chem.*, 2019, **12**, 1358–1364.
47 X. Tian, Y. Yi, P. Yang, P. Liu, L. Qu, M. Li, Y. Hu and B. Yang, High-charge density polymerized ionic networks boosting high ionic conductivity as quasi-solid electrolytes for high-voltage batteries, *ACS Appl. Mater. Interfaces*, 2019, **11**, 4001–4010.
48 L. Lee, S. Pao, A. Pathak, D. Kang and K. Lu, Membrane adsorber containing a new Sm(III)-organic framework for dye removal, *Environ. Sci.: Nano*, 2019, **6**, 1067–1076.
49 S. M. Mirvakili and I. W. Hunter, Multidirectional artificial muscles from nylon, *Adv. Mater.*, 2017, **29**, 1604734.
50 S. Zhu, J. Li, S. Dong, W. Ji, J. Nie, L. Zhu and B. Du, In-situ healing of damaged polyethersulfone ultrafiltration membranes with microgels, *J. Membr. Sci.*, 2022, **647**, 120313.
51 S. A. Baskakov, Y. V. Baskakova, E. N. Kabachkov, N. N. Dremova, A. Michtchenko and Y. M. Shulga, Novel superhydrophobic aerogel on the base of polytetrafluoroethylene, *ACS Appl. Mater. Interfaces*, 2019, **11**, 32517–32522.
52 L. Zhao, X. Song, X. Ren, H. Wang, D. Fan, D. Wu and Q. Wei, Ultrasensitive near-infrared electrochemiluminescence biosensor derived from Eu-MOF with antenna effect and high efficiency catalysis of specific CoS_2 hollow triple shelled nanoboxes for procalcitonin, *Biosensors. Bioelectron.*, 2021, **191**, 113409.
53 A. Garg, M. Almáši, J. Bednarčík, R. Sharma, V. S. Rao, P. Panchal, A. Jain and A. Sharma, Gd(III) metal–organic framework as an effective humidity sensor and its hydrogen adsorption properties, *Chemosphere*, 2022, **305**, 135467.
54 C. Lee, N. Leconte, J. Kim, D. Cho, I. Lyo and E. J. Choi, Optical spectroscopy study on the effect of hydrogen adsorption on graphene, *Carbon*, 2016, **103**, 109–114.
55 P. Wu, Q. Du, Y. Sun, Z. Li and H. He, MIP-coated Eu(BTC) for the fluorometric determination of lincomycin in eggs, *Anal. Methods*, 2019, **11**, 4501–4510.
56 X. Yang, Y. Liang, W. Feng, C. Yang, L. Wang, G. Huang and D. Wang, Hollow terbium metal–organic-framework spheres: preparation and their performance in Fe^{3+} detection, *RSC Adv.*, 2022, **12**, 4153–4161.
57 J. Chen, J. Wei, P. Zhang, X. Niu, W. Zhao, Z. Zhu, H. Ding and H. Xiong, Red-Emissive carbon dots for fingerprints detection by spray method: coffee ring effect and unquenched fluorescence in drying process, *ACS Appl. Mater. Interfaces*, 2017, **9**, 18429–18433.
58 H. Guo, Y. Zhu, S. Wang, S. Su, L. Zhou and H. Zhang, Combining coordination modulation with acid–base adjustment for the control over size of metal–organic frameworks, *Chem. Mater.*, 2012, **24**, 444–450.
59 Q. Zhao, T. Saito, K. Miyakawa, H. Sasamoto, T. Kobayashi and T. Sasaki, Sorption of Cs^+ and Eu^{3+} ions onto sedimentary rock in the presence of gamma-irradiated humic acid, *J. Hazard. Mater.*, 2022, **428**, 128211.
60 T. Lu, Y. Zhu, Y. Qi, Y. Kang and A. Wang, Tunable superporous magnetic adsorbent prepared via eco-friendly Pickering MIPEs for high-efficiency adsorption of Rb^+ and Sr^{2+}, *Chem. Eng. J.*, 2019, **368**, 988–998.
61 Z. C. Qu, C. A. Xu, Z. R. Hua, Y. Li, H. F. Meng, Z. Y. Tan, J. Shi and K. Wu, $(CF_3SO_3)_3$Er-decorated black

phosphorene for robust ambient stability and excellent flame retardancy in epoxy resin, *Composites, Part B*, 2020, **202**, 108440.

62 K. C. Jie, Y. J. Zhou, H. P. Ryan, S. Dai and J. R. Nitschke, Engineering Permanent Porosity into Liquids, *Adv. Mater.*, 2021, **33**, 20057.

63 L. P. Wang, J. He, X. Y. Chen and Y. L. Lv, A lanthanide MOF catalyst with an excellent thermal stability for the synthesis of polycarbonate diol, *J. Iran. Chem. Soc.*, 2020, **11**, 2335–2343.

64 Y. Qi, X. Xiao, Y. Q. Mei, L. Y. Z. Xiong, L. H. Chen, X. L. Lin, Z. Lin, S. R. Sun, B. Han, D. J. Yang, Y. L. Qin and X. Q. Qiu, Modulation of Brønsted and Lewis acid centers for $Ni_xCo_{3-x}O_4$ spinel catalysts: towards efficient catalytic conversion of lignin, *Adv. Funct. Mater.*, 2022, **32**, 2111615.

65 L. Kong, J. Zhang, Y. Wang, Q. Yan, J. Xu, X. Quan, C. B. Andrews, Z. Zhang and C. Zheng, Bowknot-like Zr/La bimetallic organic frameworks for enhanced arsenate and phosphate removal: combined experimental and DFT studies, *J. Colloid Interface Sci.*, 2022, **614**, 47–57.

66 M. Aghazadeh and H. Foratirad, Facile fabrication of mixed samarium/tellurium metal–organic frameworks onto Ni foam and its outstanding cycling performance as binder-free battery-type electrode for supercapacitors, *Mater. Lett.*, 2022, **313**, 3180.

67 Y. Wang, L. Zhao, J. Ma and J. Zhang, Confined interface transformation of metal–organic frameworks for highly efficient oxygen evolution reactions, *Energy Environ. Sci.*, 2022, **15**, 3830–3841.

68 H. Jin, H. Zhou, P. Ji, C. Zhang, J. Luo, W. Zeng, C. Hu, D. He and S. Mu, ZIF-8/$LiFePO_4$ derived Fe-N-P Co-doped carbon nanotube encapsulated Fe_2P nanoparticles for efficient oxygen reduction and Zn-air batteries, *Nano Res.*, 2020, **13**, 818–823.

69 Y. He, M. Liu, S. Chen and J. Zhang, Shapeable carbon fiber networks with hierarchical porous structure for high-performance Zn–I_2 batteries, *Sci. China: Chem.*, 2022, **65**, 391–398.

70 M. Ruszela, B. Grzybowska, M. Łanieckib and M. Wojtowski, Au/Ti-SBA-15 catalysts in CO and preferential (PROX) CO oxidation, *Catal. Commun.*, 2007, **8**, 1284–1286.

71 F. X. Llabrési Xamena, O. Casanova, R. G. Tailleur, H. Garcia and A. Corma, Metal organic frameworks (MOFs) as catalysts: acombination of Cu^{2+} and Co^{2+} MOFs as an efficient catalyst for tetralin oxidation, *J. Catal.*, 2008, **255**, 220–227.

72 W. C. Drinkard Jr. and J. C. Bailar, Copper Phthalocyanine Polymers1, *J. Am. Chem. Soc.*, 1959, **81**, 4795–4797.

73 K. S. Suslick, The sonochemical hot spot, *J. Acoust. Soc. Am.*, 1991, **89**, 1885–1886.

74 B. J. Gu, Z. Q. Long, X. W. Huang and H. W. Li, Present status and prospect of RE comoiund industry in China, *Rare Metals*, 2003, **03**, 391–394.

75 J. Jones, H. F. Xiong, A. T. DeLaRiva, E. J. Peterson, H. Pham, S. R. Challa, G. S. Qi, S. Oh, M. H. Wiebenga, X. I. P. Hernández, Y. Wang and A. K. Datye, Thermally stable single-atom platinum-on-ceria catalysts via atom trapping, *Science*, 2016, **353**, 6295.

76 Z. L. Wu, M. J. Li and S. H. Overbury, On the structure dependence of CO oxidation over CeO_2 nanocrystals with well-defined surface planes, *J. Catal.*, 2012, **285**, 61–73.

77 Z. P. Shao, S. M. Haile, J. Ahn, P. D. Ronney, Z. L. Zhan and S. A. Barnett, A thermally self-sustained micro solid-oxide fuel-cell stack with high power density, *Nature*, 2005, **435**, 795–798.

78 T. Ishihara, T. Shibayama, H. Nishiguchi and Y. Takita, Nickel-Gd-doped CeO_2 cermet anode for intermediate temperature operating solid oxide fuel cells using $LaGaO_3$-based perovskite electrolyte, *Solid State Ionics*, 2000, **132**, 209–216.

79 Y. C. Huanga, B. Long, M. N. Tang, Z. B. Rui, M. S. Balogunb, Y. X. Tong and H. B. Ji, Bifunctional catalytic material: an ultrastable and high-performance surface defect CeO_2 nanosheets for formaldehyde thermal oxidation and photocatalytic oxidation, *Appl. Catal., B*, 2016, **181**, 779–787.

80 T. N. Ravishankar, T. Ramakrishnappa, G. Nagaraju and H. Rajanaika, Synthesis and characterization of CeO_2 nanoparticles via solution combustion method for photocatalytic and, antibacterial activity studies, *ChemistryOpen*, 2014, **00**, 1–10.

81 S. Liu, X. D. Wu, W. Liu, W. M. Chen, R. Ran, M. Li and D. Weng, Soot oxidation over CeO_2 and Ag/CeO_2: factors determining the catalyst activity and stability during reaction, *J. Catal.*, 2016, **337**, 188–198.

82 A. Setiabudi, J. L. Chen, G. Mul, M. Makkee and J. A. Moulijn, CeO_2 catalysed soot oxidation the role factive oxygen to accelerate the oxidation conversion, *Appl. Catal., B*, 2004, **51**, 9–19.

83 M. Z. Zhu, C. Zhao, X. K. Liu, X. L. Wang, F. Y. Zhou, J. Wang, Y. M. Hu, Y. F. Zhao, T. Yao, L. M. Yang and Y. E. Wu, Single Atomic cerium sites with a high coordination number for efficient oxygen reduction in proton-exchange membrane fuel cells, *ACS Catal.*, 2021, **11**, 3923–3929.

84 F. Chen, L. Wang, Y. Xing and J. Zhang, Stable photoluminescence of lanthanide complexes in aqueous media through metal–organic frameworks nanoparticles with plugged surface, *J. Colloid Interface Sci.*, 2018, **527**, 68–77.

85 W. Gao, B. Xiang, T. T. Meng, F. Liu and X. R. Qi, Chemotherapeutic drug delivery to cancer cells using a combination of folate targeting and tumor microenvironment-sensitive polypeptides, *Biomaterials*, 2013, **34**, 4137–4149.

86 Y. J. Sang, F. F. Cao, W. Li, L. Zhang, Y. W. You, Q. Q. Deng, K. Dong, J. S. Ren and X. G. Qu, Bioinspired construction of a nanozyme-based h_2o_2 homeostasis disruptor for intensive chemodynamic Therapy, *J. Am. Chem. Soc.*, 2020, **2**, 1–8.

87 M. Xu, B. Chi, Z. Han, Y. He, F. Tian, Z. Xu, L. Li and J. Wang, Controllable synthesis of rare earth (Gd^{3+}, Tm^{3+}) doped prussian blue for multimode imaging guided synergistic treatment, *Dalton Trans.*, 2020, **49**, 12327–12337.

88 C. Wang, L. Cheng and Z. Liu, Drug delivery with upconversion nanoparticles for multi-functional targeted cancer cell imaging and therapy, *Biomaterials*, 2011, **32**, 1110–1120.
89 M. H. Guo, Y. M. Wang, B. Y. Qi, J. M. Xu, J. F. Jiang and X. C. Wang, Synthesis and Sensing Properties of ZIF-8 Derived La-doped ZnO Nanoparticles, *J. Mater. Sci. Eng.*, 2022, **01**(51–56), 128.
90 D. Guo, C. Shan, S. Qu and D. Shen, Highly sensitive ultraviolet photodetectors fabricated from ZnO quantum dots/carbon nanodots hybrid films, *Sci. Rep.*, 2014, **4**, 7469.
91 Z. Codola, L. Gomez, S. T. Kleespies, L. Q. Jr, M. Costas and J. L. Fillol, Evidence for an oxygen evolving iron-oxo-cerium intermediate in iron-catalysed water oxidation, *Nat. Commun.*, 2015, **6**, 5856.
92 G. M. Lyu, Y. J. Wang, X. Huang, H. Y. Zhang, L. D. Sun, Y. J. Liu and C. H. Yan, Hydrophilic CeO_2 nanocubes protect pancreatic β-cell line INS-1 from H_2O_2-induced oxidative stress, *Nanoscale*, 2016, **9**, 7–27.
93 B. Wang, P. Xi, C. Shan, H. Chen, H. Xu, K. Iqbal, W. Liu and Y. Tang, In situ growth of ceria on cerium-nitrogen-carbon as promoter for oxygen evolution reaction, *Adv. Mater. Interfaces*, 2017, **4**, 1700272.
94 T. Masuda, H. Fukumitsu, K. Fugane, H. Togasaki, D. Matsumura, K. Tamura, Y. Nishihata, H. Yoshikawa, K. Kobayashi, T. Mori and K. Uosaki, Role of cerium oxide in the enhancement of activity for the oxygen reduction reaction at Pt–CeO_x nanocomposite electrocatalyst-an in situ electrochemical X-ray absorption fine structure study, *J. Phys. Chem. C*, 2012, **116**, 10098–10102.
95 Y. Hou, X. Zhuang and X. Feng, Recent advances in earth-abundant heterogeneous electrocatalysts for photoelectrochemical water splitting, *Small Methods*, 2017, **1**, 1700090.
96 D. Yang, S. Mei, Z. Wen, X. Wei, Z. Cui, B. Yang, C. Wei, Y. Qiu, M. Li, H. Li, W. Zhang, F. Xie, L. Wang and R. Guo, Dual-emission of silicon nanoparticles encapsulated lanthanide-based metal–organic frameworks for ratiometric fluorescence detection of bacterial spores, *Microchim. Acta*, 2020, **187**, 666.
97 A. M. Kaczmarek, Y. Y. Liu, C. Wang, B. Laforce, L. Vincze, P. Van Der Voort and R. Van Deun, Grafting of a Eu^{3+}-tfac complex on to a Tb^{3+}-metal organic framework for use as a ratiometric thermometer, *Dalton Trans.*, 2017, **46**, 12717–12723.
98 S. Wang, X. Wu, Z. Li and C. Lu, Designed synthesis of a proton-conductive Ho-MOF with reversible dehydration and hydration, *Dalton Trans.*, 2019, **48**, 9930–9934.
99 X. Z. Wang, J. Du, N. N. Xiao, Y. Zhang, L. Fei, J. D. LaCoste, Z. Huang, Q. Wang, X. R. Wang and B. Ding, Driving force to detect Alzheimer's disease biomarkers: application of a thioflavine T@Er-MOF ratiometric fluorescent sensor for smart detection of presenilin 1, amyloid beta-protein and acetylcholine, *Analyst*, 2020, **145**, 4646–4663.
100 Y. Liu, C. Zhang, C. Xu, C. Lin, K. Sun, J. Wang, X. Chen, L. Li, A. K. Whittaker and H. Xu, Controlled synthesis of up-conversion luminescent Gd/Tm-MOFs for pH-responsive drug delivery and UCL/MRI dual-modal imaging, *Dalton Trans.*, 2018, **47**, 11253–11263.
101 X. Y. Wang, S. Y. Xiao, Z. W. Jiang, S. J. Zhen, C. Z. Huang, Q. Q. Liu and Y. F. Li, An ultrathin 2D Yb(III) metal–organic frameworks with strong electrochemiluminescence as a "on-off-on" platform for detection of picric acid and berberine chloride form, *Talanta*, 2021, **234**, 122625.
102 S. Li, S. Peng, L. Huang, X. Cui, A. M. Al-Enizi and G. Zheng, Carbon-Coated Co^{3+}-Rich Cobalt Selenide Derived from ZIF-67 for Efficient Electrochemical Water Oxidation, *ACS Appl. Mater. Interfaces*, 2016, **8**, 20534–20539.
103 H. Li, Y. Li, X. Zhang, P. Liu, M. He, C. Li and Y. Wang, Near-infrared photoactive Yb-MOF functionalized with a large conjugate ionic liquid: synthesis and application for photoelectrochemical immunosensing of carcinoma embryonic antigen, *Nanoscale*, 2021, **13**, 9757–9765.
104 X. Z. Wang, X. Y. Mao, Z. Q. Zhang, R. Guo, Y. Y. Zhang, N. J. Zhu, K. Wang, P. P. Sun, J. Z. Huo, X. R. Wang and B. Ding, Solvothermal and ultrasonic preparation of two unique cluster-based Lu and Y coordination materials: metal–organic framework-based ratiometric fluorescent biosensor for an ornidazole and ronidazole and sensing platform for a biomarker of amoeba liver abscess, *Inorg. Chem.*, 2020, **59**, 2910–2922.
105 C. Dong, M. Li, T. Yang, L. Feng, Y. Ai, Z. Ning, M. Liu, X. Lai and D. Gao, Controllable synthesis of Tb-based metal–organic frameworks as an efficient fluorescent sensor for Cu^{2+} detection, *Rare Met.*, 2021, **40**, 505–512.
106 D. Wei, Y. Xin, Y. Rong, Y. Li, C. Zhang, Q. Chen, S. Qin, W. Wang and Y. Hao, A mesoporous Gd-MOF with Lewis basic sites for 5-Fu delivery and inhibition of human lung cancer cells in vivo and in vitro, *J. Inorg. Organomet. Polym. Mater.*, 2020, **30**, 1121–1131.
107 H. Wang, C. Qian, J. Liu, Y. Zeng, D. Wang, W. Zhou, L. Gu, H. Wu, G. Liu and Y. Zhao, Integrating suitable linkage of covalent organic frameworks into covalently bridged inorganic/organic hybrids toward efficient photocatalysis, *J. Am. Chem. Soc.*, 2020, **142**, 4862–4871.
108 B. Pattengale, J. Neu, S. Ostresh, G. Hu, J. A. Spies, R. Okabe, G. W. Brudvig and C. A. Schmuttenmaer, metal–organic framework photoconductivity via time-resolved terahertz spectroscopy, *J. Am. Chem. Soc.*, 2019, **141**, 9793–9797.
109 D. Sun, M. Gu, R. Li, S. Yin, X. Song, B. Zhao, C. Li, J. Li, Z. Feng and T. Sato, Effects of nitrogen content in monocrystalline nano-CeO_2 on the degradation of dye in indoor lighting, *Appl. Surf. Sci.*, 2013, **280**, 693–697.
110 W. Lei, T. Zhang, L. Gu, P. Liu, J. A. Rodriguez, G. Liu and M. Liu, Surface-structure sensitivity of CeO_2 nanocrystals in photocatalysis and enhancing the reactivity with nanogold, *ACS Catal.*, 2015, **5**, 4385–4393.
111 Z. Ye, J. Li, M. Zhou, H. Wang, Y. Ma, P. Huo, L. Yu and Y. Yan, Well-dispersed nebula-like ZnO/CeO_2@HNTs heterostructure for efficient photocatalytic degradation of tetracycline, *Chem. Eng. J.*, 2016, **304**, 917–933.
112 I. K. Mishra, H. Zhou, J. Sun, F. Qin, K. Dahal, J. Bao, S. Chen and Z. Ren, Hierarchical CoP/Ni_5P_4/CoP microsheet

arrays as a robust pH-universal electrocatalyst for efficient hydrogen generation, *Energy Environ. Sci.*, 2018, **11**, 2246–2252.
113 B. Pattengale, J. Neu, S. Ostresh, G. Hu, J. A. Spies, R. Okabe, G. W. Brudvig and C. A. Schmuttenmaer, metal–organic framework photoconductivity via time-resolved terahertz spectroscopy, *J. Am. Chem. Soc.*, 2019, **141**, 9793–9797.
114 X. Sun, K. Yuan and Y. Zhang, Advances and prospects of rare earth metal–organic frameworks in catalytic applications, *J. Rare Earths*, 2020, **38**, 801–818.
115 R. J. Drout, L. Robison, Z. Chen, T. Islamoglu and O. K. Farha, Zirconium metal–organic frameworks for organic pollutant adsorption, *Trends Chem.*, 2019, **1**, 304–317.
116 P. A. Kobielska, A. J. Howarth, O. K. Farha and S. Nayak, metal–organic frameworks for heavy metal removal from water, *Coord. Chem. Rev.*, 2018, **358**, 92–107.
117 P. Horcajada, C. Serre, G. Maurin, N. A. Ramsahye, F. Balas, M. Vallet-Regí, M. Sebban, F. Taulelle and G. Férey, Flexible porous metal–organic frameworks for a controlled drug delivery, *J. Am. Chem. Soc.*, 2008, **130**, 6774–6780.
118 C. Orellana-Tavra, R. J. Marshall, E. F. Baxter, I. A. Lázaro, A. Tao, A. K. Cheetham, R. S. Forgan and D. Fairen-Jimenez, Drug delivery and controlled release from biocompatible metal–organic frameworks using mechanical amorphization, *J. Mater. Chem. B*, 2016, **4**, 7697–7707.
119 N. L. Rosi, J. Kim, M. Eddaoudi, B. Chen, M. O'Keeffe and O. M. Yaghi, Rod packings and metal–organic frameworks constructed from rod-shaped secondary building units, *J. Am. Chem. Soc.*, 2005, **127**, 1504–1518.
120 Y. Cui, B. Li, H. He, W. Zhou, B. Chen and G. Qian, Metal–organic frameworks as platforms for functional materials, *Acc. Chem. Res.*, 2016, **49**, 483–493.
121 Y. Cui, Y. Yue, G. Qian and B. Chen, Luminescent functional metal–organic frameworks, *Chem. Rev.*, 2012, **112**, 1126–1162.
122 T. Faust, MOFs move to market, *Nat. Chem.*, 2016, **8**, 990–991.
123 T. Faust, O. Farha and B. Hernandez, Frameworks for commercial success, *Nat. Chem.*, 2016, **8**, 987.
124 N. Joseph, H. D. Lawson, K. J. Overholt, K. Damodaran, R. Gottardi, A. P. Acharya and S. R. Little, Synthesis and characterization of CaSr-Metal Organic Frameworks for biodegradable orthopedic applications, *Sci. Rep.*, 2019, **9**, 13024.
125 L. Robison, L. Zhang, R. J. Drout, P. Li, C. R. Haney, A. Brikha, H. Noh, B. L. Mehdi, N. D. Browning, V. P. Dravid, Q. Cui, T. Islamoglu and O. K. Farha, A bismuth metal–organic framework as a contrast agent for X-ray Computed tomography, *ACS Appl. Bio Mater.*, 2019, **2**, 1197–1203.
126 X. Sun, Q. Yu, F. Zhang, J. Wei and P. Yang, A dye-like ligand-based metal–organic framework for efficient photocatalytic hydrogen production from aqueous solution, *Catal. Sci. Technol.*, 2016, **6**, 3840–3844.
127 Q. Yu, H. Dong, X. Zhang, Y. Zhu, J. Wang, F. Zhang and X. Sun, Novel stable metal–organic framework photocatalyst for light-driven hydrogen production, *CrystEngComm*, 2018, **20**, 3228–3233.
128 X. Wu, L. Gagliardi and D. G. Truhlar, Cerium metal–organic Framework for Photocatalysis, *J. Am. Chem. Soc.*, 2018, **140**, 7904–7912.
129 F. Chen, Z. Ma, L. Ye, T. Ma, T. Zhang, Y. Zhang and H. Huang, Macroscopic spontaneous polarization and surface oxygen vacancies collaboratively boosting CO_2 photoreduction on $BiOIO_3$ single crystals, *Adv. Mater.*, 2020, **32**, 1908350.
130 T. T. Zhuang, Y. Liu, M. Sun, S. L. Jiang, M. W. Zhang, X. C. Wang, Q. Zhang, J. Jiang and S. H. Yu, A unique ternary semiconductor-(semiconductor/metal) nano-architecture for efficient photocatalytic hydrogen evolution, *Angew. Chem., Int. Ed.*, 2015, **54**, 11495–11500.
131 D. M. Koshy, S. Chen, D. U. Lee, M. B. Stevens, A. M. Abdellah, S. M. Dull, G. Chen, D. Nordlund, A. Gallo, C. Hahn, D. C. Higgins, Z. Bao and T. F. Jaramillo, Understanding the origin of highly selective CO_2 electroreduction to CO on Ni,N-doped carbon catalysts, *Angew. Chem., Int. Ed.*, 2020, **59**, 4043–4050.
132 H. Wang, X. Yuan, Y. Wu, G. Zeng, X. Chen, L. Leng and H. Li, Synthesis and applications of novel graphitic carbon nitride/metal–organic frameworks mesoporous photocatalyst for dyes removal, *Appl. Catal., B*, 2015, **174–175**, 445–454.
133 L. Zhang, Z. Jin, S. Huang, Y. Zhang, M. Zhang, Y. J. Zeng and S. Ruan, Ce-doped graphitic carbon nitride derived from metal organic frameworks as a visible light-responsive photocatalyst for H_2 production, *Nanomaterials*, 2019, **9**, 1539.
134 F. Chen, Z. Ma, L. Ye, T. Ma, T. Zhang, Y. Zhang and H. Huang, Macroscopic spontaneous polarization and surface oxygen vacancies collaboratively boosting CO_2 photoreduction on $BiOIO_3$ single crystals, *Adv. Mater.*, 2020, **32**, 1908350.
135 Z. Hu and D. Zhao, metal–organic frameworks with Lewis acidity: synthesis, characterization, and catalytic applications, *CrystEngComm*, 2019, **19**, 4066–4081.
136 L. Zhu, X. Q. Liu, H. L. Jiang and L. B. Sun, Metal–organic frameworks for heterogeneous basic catalysis, *Chem. Rev.*, 2017, **117**, 8129–8176.
137 Z. Z. Jiang, Y. F. Wang, R. R. Chen, Y. Zhu, L. Zhang, S. Liu and H. L. Liu, Determination of volatile fatty acids in feces by headspace gas chromatography-mass spectrometry, *Chin. J. Anal. Chem.*, 2014, **42**, 429–435.
138 X. Yang, Z. Xie, Y. Li and Y. Zhang, Enantioselective aerobic oxidative cross-dehydrogenative coupling of glycine derivatives with ketones and aldehydes via cooperative photoredox catalysis and organocatalysis, *Chem. Sci.*, 2020, **11**, 4741–4746.
139 J. A. Chiong, J. Zhu, J. B. Bailey, M. Kalaj, R. H. Subramanian, W. Xu, S. M. Cohen and F. A. Tezcan, An exceptionally stable metal–organic framework constructed from chelate-based metal–organic polyhedra, *J. Am. Chem. Soc.*, 2020, **142**, 6907–6912.

140 Y. Su, J. Yu, Y. Li, S. Phua, G. Liu, W. Lim, X. Yang, R. Ganguly, C. Dang, C. Yang and Y. Zhao, Versatile bimetallic lanthanide metal-organic frameworks for tunable emission and efficient fluorescence sensing, *Commun. Chem.*, 2018, **1**, 12.

141 K. A. Vincent, G. J. Tilley, N. C. Quammie, I. Streeter, B. K. Burgess, M. R. Cheesman and F. A. Armstrong, Instantaneous, stoichiometric generation of powerfully reducing states of protein active sites using Eu(II) and polyaminocarboxylate ligands, *Chem. Commun.*, 2003, 2590–2591.

142 C. C. Lee, Y. Hu and M. W. Ribbe, ATP-independent substrate reduction by nitrogenase P-cluster variant, *Proc. Natl. Acad. Sci. U. S. A.*, 2012, **109**, 6922–6926.

143 Z. H. Yan, M. H. Du, J. Liu, S. Jin, C. Wang, G. L. Zhuang, X. J. Kong, L. S. Long and L. S. Zheng, Photo-generated dinuclear $\{Eu(II)\}_2$ active sites for selective CO_2 reduction in a photosensitizing metal–organic framework, *Nat. Commun.*, 2018, **9**, 3353.

144 Z. G. Zheng, C. Z. Lin and Q. Y. Chen, Di-μ-methacrylato-bis[diaquabis (methacrylato) europium(III)] methacrylic acid disolvate, *Acta Crystallogr., Sect. E: Struct. Rep. Online*, 2007, **64**, 178.

145 A. Alzamly, M. Bakiro, S. Hussein Ahmed, M. A. Alnaqbi and H. L. Nguyen, Rare-earth metal–organic frameworks as advanced catalytic platforms for organic synthesis, *Coord. Chem. Rev.*, 2020, **425**, 213543.

146 P. Wu, X. Guo, L. Cheng, C. He, J. Wang and C. Duan, Photoactive metal–organic framework and its film for light-driven hydrogen production and carbon dioxide reduction, *Inorg. Chem.*, 2016, **55**, 8153–8159.

147 H. Xu, C. S. Cao, H. S. Hu, S. B. Wang, J. C. Liu, P. Cheng, N. Kaltsoyannis, J. Li and B. Zhao, High uptake of $ReO_4(-)$ and CO_2 conversion by a radiation-resistant thorium-nickle [Th48 Ni_6] nanocage-based metal–organic framework, *Angew. Chem., Int. Ed.*, 2019, **58**, 6022–6027.

148 L. Zhang, S. Yuan, L. Feng, B. Guo, J. S. Qin, B. Xu, C. Lollar, D. Sun and H. C. Zhou, Pore-environment engineering with multiple metal sites in rare-earth porphyrinic metal–organic frameworks, *Angew. Chem., Int. Ed.*, 2018, **57**, 5095–5099.

149 L. Feng, Y. Wang, K. Zhang, K. Y. Wang, W. Fan, X. Wang, J. A. Powell, B. Guo, F. Dai, L. Zhang, R. Wang, D. Sun and H. C. Zhou, Molecular pivot-hinge installation to evolve topology in rare-earth metal–organic frameworks, *Angew. Chem., Int. Ed.*, 2019, **131**, 16835–16843.

150 W. Cai, X. Yu, Y. Cao, C. Hu, Y. Wang, Y. Zhao and Y. Bu, Electron-coupled enhanced interfacial interaction of Ce-MOF/Bi_2MoO_6 heterostructure for boosted photoreduction CO_2, *J. Environ. Chem. Eng.*, 2022, **10**, 107461.

151 Z. Li, J. Chu, D. Meng, Y. Wen, X. Xing, H. Miao, M. Hu, C. Yu, Z. Wei, Y. Yang and Y. Li, Photocatalytic chemical CO_2 fixation by Cu-BDC nanosheet@macroporous–mesoporous-TiO_2 under mild conditions, *ACS Catal.*, 2019, **9**, 8659–8668.

152 M. Hu, J. Liu, S. Song, W. Wang, J. Yao, Y. Gong, C. Li, H. Li, Y. Li, X. Yuan, Z. Fang, H. Xu, W. Song and Z. Li, Ultra-thin two-dimensional trimetallic metal–organic framework for photocatalytic reduction of CO_2, *ACS Catal.*, 2022, **12**, 3238–3248.

153 S. Wu, X. Xing, D. Wang, J. Zhang, J. Chu, C. Yu, Z. Wei, M. Hu, X. Zhang and Z. Li, Highly ordered hierarchically macroporous MIL-125 with high specific surface area for photocatalytic CO_2 fixation, *ACS Sustainable Chem. Eng.*, 2019, **8**, 148–153.

154 C. Pagis, M. Ferbinteanu, G. Rothenberg and S. Tanase, Lanthanide-based metal organic frameworks: synthetic strategies and catalytic applications, *ACS Catal.*, 2016, **6**, 6063–6072.

155 C. Du, Z. Zhang, G. Yu, H. Wu, H. Chen, L. Zhou, Y. Zhang, Y. Su, S. Tan, L. Yang, J. Song and S. Wang, A review of metal organic framework (MOFs)-based materials for antibiotics removal via adsorption and photocatalysis, *Chemosphere*, 2021, **272**, 129501.

156 Y. Qiao and E. J. Schelter, Lanthanide photocatalysis, *Acc. Chem. Res.*, 2018, **51**, 2926–2936.

157 D. Zhao and C. Cai, Adsorption and photocatalytic degradation of pollutants on Ce-doped MIL-101-NH_2/Ag_3PO_4 composites, *Catal. Commun.*, 2020, **136**, 105910.

158 F. Wang, Y. Pu, X. Zhang, F. Zhang, H. Cheng and Y. Zhao, A series of multifunctional lanthanide metal–organic frameworks for luminescent sensing and photocatalytic applications, *J. Lumin.*, 2019, **206**, 192–198.

159 W. Wu, W. Liu, X. Shen, H. Zhong, J. Xu, B. Li, J. Q. Liu, A. K. Singh, A. Singh and A. Kumar, A new 3D Gd-based metal–organic framework with paddle-wheel unit: structure and photocatalytic property, *Inorg. Chem. Commun.*, 2018, **95**, 104–106.

160 X. Lian and B. Yan, A postsynthetic modified MOF hybrid as heterogeneous photocatalyst for alpha-phenethyl alcohol and reusable fluorescence sensor, *Inorg. Chem.*, 2016, **55**, 11831–11838.

161 Z. W. Jiang, Y. C. Zou, T. T. Zhao, S. J. Zhen, Y. F. Li and C. Z. Huang, Controllable synthesis of porphyrin-based 2D lanthanide metal–organic frameworks with thickness- and metal-node-dependent photocatalytic performance, *Angew. Chem., Int. Ed.*, 2020, **59**, 3300–3306.

162 R. Kaur, K. Vellingiri, K. H. Kim, A. K. Paul and A. Deep, Efficient photocatalytic degradation of rhodamine 6G with a quantum dot-metal organic framework nanocomposite, *Chemosphere*, 2016, **154**, 620–627.

163 W. Pan, C. Gong, X. Zeng, C. Hu, Y. Zhang, D.-R. Zhu, H. Xu, H. Guo, J. Zhang and J. Xie, Assembly of porous lanthanide metal–organic frameworks constructed by chalcone dicarboxylic acid and exploration of their properties, *Polyhedron*, 2019, **169**, 24–31.

164 L. M. Aguirre-Diaz, N. Snejko, M. Iglesias, F. Sanchez, E. Gutierrez-Puebla and M. A. Monge, Efficient rare-earth-based coordination polymers as green photocatalysts for the synthesis of imines at room temperature, *Inorg. Chem.*, 2018, **57**, 6883–6892.

165 Z. W. Jiang, T. T. Zhao, S. J. Zhen, C. M. Li, Y. F. Li and C. Z. Huang, A 2D MOF-based artificial light-harvesting

system with chloroplast bionic structure for photochemical catalysis, *J. Mater. Chem. A*, 2021, **9**, 9301–9306.

166 C. Zhang, L. Ai and J. Jiang, Solvothermal synthesis of MIL–53(Fe) hybrid magnetic composites for photoelectrochemical water oxidation and organic pollutant photodegradation under visible light, *J. Mater. Chem. A*, 2015, **3**, 3074–3081.

167 J. Zhao, W. W. Dong, Y. P. Wu, Y.-N. Wang, C. Wang, D. S. Li and Q. C. Zhang, Two (3,6)-connected porous metal–organic frameworks based on linear trinuclear $[Co_3(COO)_6]$ and paddlewheel dinuclear $[Cu_2(COO)_4]$ SBUs: gas adsorption, photocatalytic behaviour, and magnetic properties, *J. Mater. Chem. A*, 2015, **3**, 6962–6969.

168 J. Gao, J. Miao, P. Z. Li, W. Y. Teng, L. Yang, Y. Zhao, B. Liu and Q. Zhang, A p-type Ti(IV)-based metal–organic framework with visible-light photo-response, *Chem. Commun.*, 2014, **50**, 3786–3788.

169 Y. L. Hou, R. W. Sun, X. P. Zhou, J. H. Wang and D. Li, A copper(I)/copper(II)-salen coordination polymer as a bimetallic catalyst for three-component Strecker reactions and degradation of organic dyes, *Chem. Commun.*, 2014, **50**, 2295–2297.

170 Q. Xia, X. Yu, H. Zhao, S. Wang, H. Wang, Z. Guo and H. Xing, Syntheses of novel lanthanide metal–organic frameworks for highly efficient visible-light-driven dye degradation, *Cryst. Growth Des.*, 2017, **17**, 4189–4195.

171 L. M. Aguirre-Díaz, N. Snejko, M. Iglesias, F. Sánchez, E. Gutiérrez-Puebla and M. Á. Monge, Efficient Rare-Earth-Based Coordination Polymers as Green Photocatalysts for the Synthesis of Imines at Room Temperature, *Inorg. Chem.*, 2018, **57**, 6883–6892.

172 C. Zhang, Y. Xu, C. Lv, X. Zhou, Y. Wang, W. Xing, Q. Meng, Y. Kong and G. Chen, Mimicking π Backdonation in Ce-MOFs for Solar-Driven Ammonia Synthesis, *ACS Appl. Mater. Interfaces*, 2019, **11**, 29917–29923.

173 X. Shi, B. Cao, J. Liu, J. Zhang and Y. Du, Rare-earth-based metal–organic frameworks as multifunctional platforms for catalytic conversion, *Small*, 2021, **17**, 2005371.

174 F. Saraci, V. Quezada-Novoa, P. R. Donnarumma and A. J. Howarth, Rare-earth metal–organic frameworks: from structure to applications, *Chem. Soc. Rev.*, 2020, **49**, 7949–7977.

175 M. Xue, Y. Wei and G. Liu, Facile hydrothermal preparation of edge-oriented Cu_2MoS_4 as an efficient electrocatalyst for hydrogen evolution reaction, *Mater. Lett.*, 2019, **256**, 126663.

176 L. Xiong, J. Bi, L. Wang and S. Yang, Improving the electrocatalytic property of CoP for hydrogen evolution by constructing porous ternary CeO_2–CoP–C hybrid nanostructure via ionic exchange of MOF, *Int. J. Hydrogen Energy*, 2018, **43**, 20372–20381.

177 Q. Lan, Y. Lin, Y. Li and D. Liu, MOF-derived, CeO_x-modified CoP/carbon composites for oxygen evolution and hydrogen evolution reactions, *J. Mater. Sci.*, 2018, **53**, 12123–12131.

178 M. Wen, Y. Kuwahara, K. Mori, D. Zhang, H. Li and H. Yamashita, Synthesis of Ce ions doped metal–organic framework for promoting catalytic H_2 production from ammonia borane under visible light irradiation, *J. Mater. Chem. A*, 2015, **3**, 14134–14141.

179 G. Han, Y. Jin, R. A. Burgess, N. E. Dickenson, X. Cao and Y. Sun, Visible-light-driven valorization of biomass intermediates integrated with H_2 production catalyzed by ultrathin Ni/CdS nanosheets, *J. Am. Chem. Soc.*, 2017, **139**, 15584–15587.

180 N. O'Brian, A. Grübler, N. Nakicenovic, M. Obersteiner, K. Riahi, L. Schrattenholzer and F. Toth, Planning for future energy resources, *Science*, 2003, **300**, 581–584.

181 B. M. Hunter, J. D. Blakemore, M. Deimund, H. B. Gray, J. R. Winkler and A. M. Muller, Highly active mixed-metal nanosheet water oxidation catalysts made by pulsed-laser ablation in liquids, *J. Am. Chem. Soc.*, 2014, **136**, 13118–13121.

182 H. Han, Z. Bai, T. Zhang, X. Wang, X. Yang, X. Ma, Y. Zhang, L. Yang and J. Lu, Hierarchical design and development of nanostructured trifunctional catalysts for electrochemical oxygen and hydrogen reactions, *Nano Energy*, 2019, **56**, 724–732.

183 G. Li, S. Zhao, Y. Zhang and Z. Tang, metal–organic frameworks encapsulating active nanoparticles as emerging composites for catalysis: recent progress and perspectives, *Adv. Mater.*, 2018, **30**, 1800702.

184 K. Chen, Z. Sun, R. Fang, Y. Shi, H. M. Cheng and F. Li, metal–organic frameworks (MOFs)-derived nitrogen-doped porous carbon anchored on graphene with multifunctional effects for lithium-sulfur batteries, *Adv. Funct. Mater.*, 2018, **19**, 1707592.

185 Y. Kuang, J. Xu, C. Wang, T. Li, S. Gai, F. He, P. Yang and J. Lin, Fine-tuning Ho-based red-upconversion luminescence by altering $NaHoF_4$ core size and $NaYbF_4$ shell thickness, *Chem. Mater.*, 2019, **31**, 7898–7909.

186 J. Liao, Z. Xue, H. Sun, F. Xue, Z. Zhao, X. Wang, W. Dong, D. Yang and M. Nie, MoS_2 supported on Er-MOF as efficient electrocatalysts for hydrogen evolution reaction, *J. Alloys Compd.*, 2022, **898**, 162991.

187 F. Liu, H. Peng, Y. Kang, Y. Hao, L. Li, H. Xin, H. Kang, W. Wang and Z. Lei, Rare-earth-based bimetallic metal–organic frameworks promote oxygen electrocatalysis for rechargeable Zn-Air batteries, *ACS Sustainable Chem. Eng.*, 2022, **10**, 10978–10988.

188 J. Liao, Z. Xue, H. Sun, F. Xue, Z. Zhao, X. Wang, W. Dong, D. Yang and M. Nie, MoS_2 supported on Er-MOF as efficient electrocatalysts for hydrogen evolution reaction, *J. Alloys Compd.*, 2022, **898**, 162991.

189 L. Xiong, J. Bi, L. Wang and S. Yang, Improving the electrocatalytic property of CoP for hydrogen evolution by constructing porous ternary CeO_2–CoP–C hybrid nanostructure via ionic exchange of MOF, *Int. J. Hydrogen Energy*, 2018, **43**, 20372–20381.

190 Q. Lan, Y. Lin, Y. Li and D. Liu, MOF-derived, CeO_x-modified CoP/carbon composites for oxygen evolution and hydrogen evolution reactions, *J. Mater. Sci.*, 2018, **53**, 12123–12131.

191 J. Zhang, J. Chen, Y. Luo, Y. Chen, C. Zhang, Y. Luo, Y. Xue, H. Liu, G. Wang and R. Wang, Engineering heterointerfaces coupled with oxygen vacancies in lanthanum-based hollow microspheres for synergistically enhanced oxygen electrocatalysis, *J. Energy Chem.*, 2021, **60**, 503–511.

192 Y. Ma, G. Mu, Y. Miao, D. Lin, C. Xu, F. Xie and W. Zeng, Hydrangea flower-like nanostructure of dysprosium-doped Fe-MOF for highly efficient oxygen evolution reaction, *Rare Met.*, 2022, **41**, 844–850.

193 Z. Wan, Q. He, J. Chen, T. T. Isimjan, B. Wang and X. Yang, Dissolution-regrowth of hierarchical Fe-Dy oxide modulates the electronic structure of nickel-organic frameworks as highly active and stable water splitting electrocatalysts, *Chin. J. Catal.*, 2020, **41**, 1745–1753.

194 F. Li, M. Jiang, C. Lai, H. Xu, K. Zhang and Z. Jin, Yttrium- and Cerium-codoped ultrathin metal–organic framework nanosheet arrays for high-efficiency electrocatalytic overall water splitting, *Nano Lett.*, 2022, **22**, 7238–7245.

195 S. Nitopi, E. Bertheussen, S. B. Scott, X. Liu, A. K. Engstfeld, S. Horch, B. Seger, I. E. L. Stephens, K. Chan, C. Hahn, J. K. Nørskov, T. F. Jaramillo and I. Chorkendorff, Progress and perspectives of electrochemical CO_2 reduction on copper in aqueous electrolyte, *Chem. Rev.*, 2019, **119**, 7610–7672.

196 A. Seifitokaldani, C. M. Gabardo, T. Burdyny, C. Dinh, J. P. Edwards, M. G. Kibria, O. S. Bushuyev, S. O. Kelley, D. Sinton and E. H. Sargent, Hydronium-induced switching between CO_2 electroreduction pathways, *J. Am. Chem. Soc.*, 2018, **140**, 3833–3837.

197 R. J. Lim, M. Xie, M. A. Sk, J. Lee, A. Fisher, X. Wang and K. H. Lim, A review on the electrochemical reduction of CO_2 in fuel cells, metal electrodes and molecular catalysts, *Catal. Today*, 2014, **233**, 169–180.

198 Y. Zheng, A. Vasileff, X. Zhou, Y. Jiao, M. Jaroniec and S. Qiao, Understanding the roadmap for electrochemical reduction of CO_2 to multi-carbon oxygenates and hydrocarbons on copper-based catalysts, *J. Am. Chem. Soc.*, 2019, **141**, 7646–7659.

199 L. Zhang, Z. Zhao and J. Gong, Nanostructured materials for heterogeneous electrocatalytic CO_2 reduction and their related reaction mechanisms, *Angew. Chem., Int. Ed.*, 2017, **56**, 11326–11353.

200 C. Yang, Y. Wang, L. Qian, A. M. Al-Enizi, L. Zhang and G. Zheng, Heterogeneous electrocatalysts for CO_2 reduction, *ACS Appl. Energy Mater.*, 2021, **4**, 1034–1044.

201 O. S. Bushuyev, P. De Luna, C. T. Dinh, L. Tao, G. Saur, J. van de Lagemaat, S. O. Kelley and E. H. Sargent, what should we make with CO_2 and how can we make it?, *Joule*, 2018, **2**, 825–832.

202 X. Duan, J. Xu, Z. Wei, J. Ma, S. Guo, S. Wang, H. Liu and S. Dou, Metal-free carbon materials for CO_2 electrochemical reduction, *Adv. Mater.*, 2017, **29**, 1701784.

203 P. De Luna, W. Liang, A. Mallick, O. Shekhah, F. P. Garcia de Arquer, A. H. Proppe, P. Todorovic, S. O. Kelley, E. H. Sargent and M. Eddaoudi, metal–organic framework thin films on high-curvature nanostructures toward tandem electrocatalysis, *ACS Appl. Mater. Interfaces*, 2018, **10**, 31225–31232.

204 D. H. Nam, O. Shekhah, G. Lee, A. Mallick, H. Jiang, F. Li, B. Chen, J. Wicks, M. Eddaoudi and E. H. Sargent, Intermediate binding control using metal–organic frameworks enhances electrochemical CO_2 reduction, *J. Am. Chem. Soc.*, 2020, **142**, 21513–21521.

205 Q. Wang, Z. Liu, H. Zhao, H. Huang, H. Jiao and Y. Du, MOF-derived porous Ni_2P nanosheets as novel bifunctional electrocatalysts for the hydrogen and oxygen evolution reactions, *J. Mater. Chem. A*, 2018, **6**, 18720–18727.

206 J. Li, G. Zhao, H. Zhao, N. Zhao, L. Lu, N. Liu, M. Wang, C. Ma, Q. Zhang and Y. Du, Cerium-doped bimetal organic framework as a superhigh capacity cathode for rechargeable alkaline batteries, *Nanoscale*, 2021, **13**, 3581–3587.

207 J. Li, H. Zhao, J. Wang, N. Li, M. Wu, Q. Zhang and Y. Du, Interplanar space-controllable carboxylate pillared metal organic framework ultrathin nanosheet for superhigh capacity rechargeable alkaline battery, *Nano Energy*, 2019, **62**, 876–882.

208 J. Xia, Y. Xue, B. Lei, L. Xu, M. Sun, N. Li, H. Zhao, M. Wang, M. Luo, C. Zhang, B. Huang, Y. Du and C. Yan, Multimodal channel cancer chemotherapy by 2D functional gadolinium metal–organic framework, *Natl. Sci. Rev.*, 2021, **8**, a221.